Direct coupled reservoir-wellbore modeling approach for the Berlín Geothermal Field, El Salvador

José Erick Jiménez Majano

June 2022

M.Sc. thesis
in Mechanical Engineering

FACULTY OF INDUSTRIAL ENGINEERING, MECHANICAL ENGINEERING AND COMPUTER SCIENCE

Direct coupled reservoir-wellbore modeling approach for the Berlín Geothermal Field, El Salvador

José Erick Jiménez Majano

60 ECTS thesis submitted in partial fulfillment of a
Magister Scientiarum degree in Mechanical Engineering

Supervisors
Andri Arnaldsson
Halldór Pálsson
Magnús Þór Jónsson
Jean-Claude Berthet

Examiner
Gunnar Gunnarsson

Faculty of Industrial Engineering, Mechanical Engineering and Computer Science
School of Engineering and Natural Sciences
University of Iceland
Reykjavik, June 2022

Direct coupled reservoir-wellbore modeling approach for the Berlín Geothermal Field, El Salvador

60 ECTS thesis submitted in partial fulfillment of a M.Sc. degree in Mechanical Engineering

To my parents, for their encouragement and dedication

Abstract

The Berlin Geothermal Field in El Salvador is used for power generation purposes with an installed capacity of 109.2 MW and delivering by 2021, 14.75% of the total energy generation in the country. In this study a numerical model for the geothermal system was developed based on a current conceptual model using a direct coupled reservoir-wellbore modeling approach implemented with the simulators TOUGH2 and FLOWELL. The purpose is to predict the reservoir response to different production scenarios. It is calibrated against formation conditions and 30 years of production data, including pressure drawdown and flowing enthalpy time series. Parameter estimation was carried out through inverse modeling using iTOUGH2 and a sensitivity analysis showed that the horizontal permeability for the main geothermal reservoir and cap-rock rock produce the most impact on the overall calibration of the system. The wellbore simulator was essential during the forecasting stage as it compensates for the mass flow rate yield from each feedzone due to pressure drawdown in the system, allowing to locate future make-up wells properly over time. The production scenarios estimate it is possible to maintain the current power generation for the next 30 years with the proper drilling program of about one make-up well every 2 years.

Útdráttur

Berlin jarðhitasvæðið í El Salvador er nýtt til raforkuframleiðslu sem gefur af sér 109.2 MW, sem er 14.75% af heildarframleiðslu landsins. Í þessu verkefni var bygg á núverandi hugmyndalíkani og tölulegt líkan af jarðhitakerfinu þróað, tengt hermunarlíkani fyrir borholur, með verkfærunum TOUGH2 og FLOWELL. Tilgangurinn er að spá fyrir um hegðun jarðhitakerfisins við mismunandi nýtingarferli. Líkanið er stillt af út frá jarðfræðiupplýsingum ásamt mælingum úr 30 ára nýtingarsögu, sem innihalda upplýsingar um þrýsti- og vermisbreytingar. Mat á stikum var framkvæmt með verkfærinu iTOUGH2 og næmnigreining sýndi að lárétt lekt bergs hafði mest áhrif á niðurstöður líkansins. Notkun hermilíkans fyrir borholur reyndist lykilatriði við að spá fyrir um framtíðarhegðun, þar sem það tekur tillit til mismunandi innflæðis í borholur á mismunandi stöðum, og þannig hægt að meta heppilega staðsetningu nýrra borhola á svæðinu. Samvæmt mati er mögulegt að viðhalda núverandi orkuframleiðslu á svæðinu næstu 30 ár með því að bæta við u.þ.b. einni borholu á tveggja ára fresti.

Contents

Contents

List of Figures

LIST OF FIGURES

List of Tables

Abbreviations

BGF   Berlin Geothermal Field

EOS   Equation Of State

MA   Moving Averarage

masl   Meters above the sea level

mbsl   Meters below the sea level

MW   Megawatt

P&T   Pressure and Temperature

TLC   Total Loss Circulation

WHP   Well Head Pressure

Nomenclature

Variables

g	Gas
α	Void fraction
β	Mass phase
$\dot{m}$	Mass flow rate
ϵ	Convergence tolerance
η	Simplicity factor
Γ	Surface area
γ	Reduction factor
κ	Mass component
λ	Enthalpy
μ	Dynamic Viscosity
Φ	Friction correction factor
ϕ	Porosity
ρ	Density
A	Area
C	Specific heat
d	Diameter
F	Mass or heat flux
f	Friction factor
h	Enthalpy

Nomenclature

k	Permeability or time level
l	Liquid
M	Mass per volumen
n	Normal direction
P	Pressure
PI	Productivity Index
q	Mass generation rate
R	Residual
S	Fluid saturation or Objective Function
T	Temperature
t	Time
u	Specific internal energy or velocity
V	Volume
X	Mass fraction
x	Steam quality
z	Vertical direction

Vectors

$\boldsymbol{C}_{zz}$	Covariance matrix of measurement errors
$\boldsymbol{z}^*$	Observation data vector
$\boldsymbol{g}$	Gravity or gas
$\boldsymbol{z}$	Model output vector

Acknowledgments

1. Introduction

The world is in a transition to renewable energy in order to assure energy sustainability for future generations; such a goal is listed and stated on the Sustainable Development Goals by the United Nations [59]. Geothermal energy offers some of the main components to make it a valid candidate to achieve the stated goal as it provides stable energy and low CO2 emissions [15]. It is a form of heat coming from below the Earth's solid surface, and its occurrence is spread around the world [3]. Nevertheless, the tectonic plate boundaries provide the geological setting to make its exploitation feasible and attractive different countries, such as the case along the Ring of Fire which stores for more than 40% of the geothermal resources in the world [38].

Geothermal energy projects have a long development time, unlike fossil-based energy projects due to the intense exploration and risk involved in assessing the resource; during production, the regulators and plant operators usually wonder about the possible expansions or depletion of the resource [1, 53]. By gathering quantitative data from geoscience collected by geophysical measurements and fluid collection, petrophysical properties and thermodynamic conditions such as pressure and temperature, a combined understanding of the geothermal system can be achieved and served as an input for the developing of a coherent computational representation of the system.

Due to the complexity of the phenomena involved in the geothermal reservoir, the usual approach is to use a numerical simulator to discretize the space and time and reproduce the measured values in the system. Such models serve to understand the system, estimate production capacity and system response to production [23]. However, they are time-consuming and computationally demanding. The more data is used to calibrate a model, the more reliable it becomes. Therefore, coupled reservoir and wellbore simulator are preferable since data collected daily, such as wellhead pressure, can be directly used for calibration.

In this study, a numerical model for the Berlin Geothermal Field in El Salvador is developed. It is calibrated using a vast amount of data that 30 years of energy production provides. TOUGH2 [45] is used as a reservoir simulator, and the built-in wellbore simulator FLOWELL [22], along with iTOUGH2 [18] parameter estimation and sensitivity analysis are performed to find the closest values for permeability,

1

porosity, and boundary conditions to match the geothermal system setting and response. This study also aims to develop and explore the evolution of the steam cap on the southern area of the BGF, evaluate the field response to long-term production, and use the model as a managing tool for future field expansions.

The study is divided into seven chapters. Chapter 2 describes the governing equations and the numerical methods used by the numerical simulator TOUGH2 and FLOWELL. Chapter 3 provides an overview of the Berlin Geothermal Field, including field development and the current conceptual model. Chapter 4 presents the model setup, simulator settings, and data handling methods used. Chapter 5 shows the model calibration, results, and forecasting. Chapters 6 and 7 focus on interpreting results, including the discussion and concluding remarks.

2. Theoretical Background

Mathematical modeling is a common practice for planning and managing geothermal fields. The numerical solution of complex non-linear partial differential equations has become more viable over time and many simulators have been developed since early 1980s, such as STAR [43], FEFLOW [58], ECLIPSE [42], TETRAD [54], TOUGH2 [44] OpenGeoSys [32], Waiwera [12], among others. However, TOUGH2 has been used over the decades in many geothermal fields around the world, and it is currently considered the state of the art simulator for multicomponent and multiphase, nonisothermal flows in porous and fractured media [45, 41]. This chapter introduces the physical theory and mathematical methods implemented by TOUGH2, iTOUGH2, and FloWell as presented by their developers Pruess (1991), Finsterle (2007,) and Guðmundsdóttir (2012).

2.1. Numerical modeling

2.1.1. Mass and Energy Balances

TOUGH2 solves the following mass and energy balance equation by integrating over an arbitrary sub-domain:

$$\frac{d}{dt} \int_{V_n} M^\kappa \, dV_n = \int_{\Gamma_n} \boldsymbol{F}^\kappa \cdot \boldsymbol{n} \, d\Gamma_n + \int_{V_n} q^\kappa \, dV_n \tag{2.1}$$

The volume V_n is bounded by a surface Γ_n. M represents the energy or mass per volume, whereas κ values range from 1 to NK, accounting for the mass components. $NK + 1$ represents the particular case of a heat component. The inner product of the mass or heat flux ($\boldsymbol{F}$) and the normal vector on the surface element $d\Gamma_n$ is represented by the first term on the left side of the equation. At the same time, the second term describes the sinks and sources (q) on the element.

The following expression represents the mass accumulation term:

2. Theoretical Background

$$M^{\kappa} = \phi \sum_{\beta} S_{\beta} \rho_{\beta} X_{\kappa}^{\beta} \tag{2.2}$$

The mass from every component κ is calculated by adding each of the fluid phases content on the porous volume, expressed by the product of β, porosity ϕ, a saturation of phase S_{β}, the density of phase ρ_{β} and the mass fraction of component κ in phase β. For the heat accumulation term in a multiphase system, the heat on the host rock is included:

$$M^{NK+1} = (1 - \phi)\rho_R C_R T + \phi \sum_{\beta} S_{\beta} \rho_{\beta} u_{\beta} \tag{2.3}$$

The first term on the right side represents the energy content on the rock, having ρ_R as rock density and C_p as rock specific heat. The second term describes the energy content on the fluid for each phase β using the specific internal energy u_{β}. The advective mass flux is calculated as a sum over phases:

$$\left. \boldsymbol{F}^{\kappa} \right|_{adv} = \sum_{\beta} X_{\beta}^{\kappa} \boldsymbol{F}_{\beta} \tag{2.4}$$

Where Darcy's law is applied and the driven force represented by the pressure gradient and the gravitational force ($\boldsymbol{g}$)

$$\boldsymbol{F}_{\beta} = -k \frac{k_{r\beta} \rho_{\beta}}{\mu_{\beta}} (\nabla P_{\beta} - \rho \boldsymbol{g}) \tag{2.5}$$

where k is the absolute permeability, $k_{r\beta}$ the relative permeability and μ_{β} the viscosity of phase β. Finally, the heat component considers conductive and convective components:

$$\boldsymbol{F}^{NK+1} = -\lambda \nabla T + \sum_{\beta} h_{\beta} \boldsymbol{F}_{\beta} \tag{2.6}$$

where λ represents the thermal conductivity and h_{β} the specific enthalpy. For this study, EOS 1 is used. Therefore, the number of components is one, and the mass transport does not consider the diffusion component.

2.1.2. Space and Time Discretization

TOUGH2 uses the integral finite difference method to solve the energy-mass balance equation, the Equation 2.1 is discretized as follows:

$$\int_{V_n} M\, dV = V_n M_n \qquad (2.7)$$

Where M_n is the average mass or energy content value over the normalized volume V_n. The first term on the right side of Equation 2.1, becomes a discrete sum of averages over the normal surfaces A_{mn}.

$$\int_{\Gamma_n} \boldsymbol{F}^\kappa \cdot \boldsymbol{n}\, d\Gamma_n = \sum_m A_{nm} F_{nm} \qquad (2.8)$$

The normal component of $\boldsymbol{F}$ is expressed as F_{nm}, A_{nm} represents the normal area between two elements V_n and V_m as shown in Figure 2.1
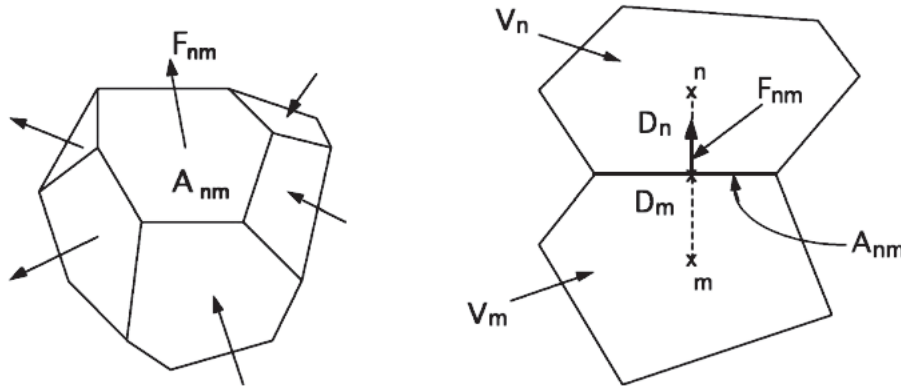
Figure 2.1: Space discretization and geometry data in the integral finite difference method [45].

The Equation 2.5 is discretized in terms of averages found on each of the elements V_n and V_m:

$$F_{\beta,nm} = -k\left[\frac{k_{r\beta}\rho_\beta}{\mu_\beta}\right]_{nm}\left[\frac{P_{\beta,n} - P_{\beta,m}}{D_{nm}} - \rho_{\beta,nm}g_{nm}\right] \qquad (2.9)$$

D_{nm} represents the nodal distance between element, $D_n + D_m$, g_m is the gravitational component between the two elements, by substituting Equations 2.8 and 2.9 into

Equation 2.1, the first-order ordinary differential equation is found:

$$\frac{dM_n^\kappa}{dt} = \frac{1}{V_n} \sum_m A_{mn} F_{nm}^\kappa + q_n^\kappa \tag{2.10}$$

The right side of Equation 2.10 is evaluated at a new time level, $t^{k+l} = t^k + \Delta t$, given the form of an implicit scheme and numerical stability, resulting in the next expression:

$$R_n^{\kappa,k+1} = M_n^{\kappa,k+1} - M_n^{\kappa,k} - \frac{\Delta t}{V_n}[\sum_m A_{nm} F_{nm}^{\kappa,k+1} + V_n q_n^{\kappa,k+1}] \tag{2.11}$$

The expression introduces the concept of residual R. The computational complexity is proportional to the number of components $NEQ = NK + 1$ times the number of elements (NEL). Each equation is solved by Newton/Raphson iteration method. Tracking the iteration with the index p, using Taylor series and retaining up to first-order elements. A set of linear equations is obtained:

$$-\sum_i \frac{\partial R_n^{\kappa,k+1}}{\partial x_i}\bigg|_p (x_{i,p+1} - x_{i,p}) = R_n^{\kappa,k+1}(x_{i,p}) \tag{2.12}$$

The first term on the right is the Jacobian matrix, which is evaluated by numerical differentiation. The iteration continues until the residuals $R_n^{\kappa,k+1}$ are smaller than an established convergence tolerance:

$$\left| \frac{R_{n,p+1}^{\kappa,k+1}}{M_{n,p+1}^{\kappa,k+1}} \right| <= \epsilon_1 \tag{2.13}$$

Convergence is usually achieved between 3 to 4 iterations. However, if the convergence criteria are not attained after a defined number of iterations, the time step δt is reduced, and the new iteration starts over.

2.2. Wellbore simulator

Wellhead conditions are collected on a daily basis in most of the geothermal fields. Hence, the model accuracy is enhanced by using field data such as wellhead pressure,

mass flow rate and flowing enthalpy. Furthermore, a wellbore-reservoir interaction enables the production to falls off as the pressure drawdown increases [8]. FLOW-ELL is a wellbore simulator for a one-dimensional, non-isothermal, steady flow of pure water under single or two-phase conditions. It was initially developed by Guð-mundsdóttir (2012) and subsequently added to the TOUGH2 [22].

2.2.1. Governing Equations

The governing equations are described by the continuity, energy, and momentum equation for single and two-phase flow. For a single-phase flow, the continuity equation can be written as:

$$u(\frac{\partial \rho}{\partial p}\frac{dp}{dz} + \frac{\partial \rho}{\partial h}\frac{dh}{dz}) + \rho\frac{du}{dz} = 0 \tag{2.14}$$

Where the u represents the velocity, ρ the density, z the vertical coordinate, and h the enthalpy, the second expression, involves kinetic, gravitational, and thermal energy:

$$\dot{m}u\frac{du}{dz} + \dot{m}\frac{dh}{dz} + \dot{m}g + \dot{Q} = 0 \tag{2.15}$$

The momentum equation involves the inertia, pressure changes, hydrostatic pressure, and head loss:

$$\rho u\frac{du}{dz} + \frac{dp}{dz} + \rho g + \frac{\rho f}{2d}|u|u = 0 \tag{2.16}$$

Where f denotes the friction factor. For the two-phase flow conditions the Equations 2.14, 2.15 and 2.16 are affected by the ratio of vapor occupying the pipe cross section, the void factor α, and liquid u_l and vapor u_g phase velocities. The different velocities are expressed in terms of a uniform velocity which represents the flow velocity assuming a saturated liquid:

$$u = \frac{q_l + q_g}{\rho_l A} \tag{2.17}$$

$$\alpha = \frac{A_g}{A_l + A_g} \tag{2.18}$$

7

2. Theoretical Background

Where A represents the cross-sectional area and the subscripts l and g, liquid and steam respectively and q the mass flow rate.

$$u_l = \frac{1-x}{1-\alpha}u \tag{2.19}$$

$$u_g = \frac{x\rho_l}{\alpha\rho_g}u \tag{2.20}$$

For steady a state and a constant diameter, the mass balance for a single-phase is expressed:

$$u\frac{\partial\rho_l}{\partial p}\frac{dp}{dz} + \rho_l\frac{du}{dz} = 0 \tag{2.21}$$

Subsequently, the energy equation for two-phase can be defined as:

$$\gamma u\frac{du}{dz} + \frac{u^2}{2}\frac{\partial\gamma}{\partial h}\frac{dp}{dz} + (1 + \frac{u^2}{2}\frac{\partial\gamma}{\partial h})\frac{dh}{dz} + g + \frac{\dot{Q}}{\dot{m}} \tag{2.22}$$

where γ denotes:

$$\gamma = \frac{(1-x)^3}{(1-\alpha)^2} + \frac{\rho_l^2}{\rho_g^2}\frac{x^3}{\alpha^2} \tag{2.23}$$

Finally, the momentum equation can be written as:

$$\eta\rho_l u\frac{du}{dz} + (1 + \rho_l u^2\frac{\partial\eta}{\partial p} + \eta u^2\frac{\partial\rho_l}{\partial p})\frac{dp}{dz} +$$
$$\rho_l u^2\frac{\partial\eta}{\partial h}\frac{dh}{dz} + ((1-\alpha)\rho_l + \alpha\rho_g)g + \frac{\rho_l\Phi^2 f}{2d}|u|u = 0 \tag{2.24}$$

where Φ^2 is the friction correction factor for the single phase pressure drop and η is defined as:

$$\eta = \frac{(1-x)^2}{1-\alpha} + \frac{\rho_l}{\rho_g}\frac{x^2}{\alpha} \tag{2.25}$$

The wellbore simulator is linked to the TOUGH2 simulator by the enthalpy and pressure encountered at the feedzone. By using the deliverability approach, where the difference between the bottom hole pressure and the pressure on phase β is directly related to the mass flow rate of the phase β through the productivity index PI:

$$P_{wb} = -\frac{q_\beta}{PI}\frac{\mu_\beta}{k_{r\beta}\rho_\beta} + P_\beta \tag{2.26}$$

Where $k_{r\beta}$ represents the relative permeability of the phase β. The simulator can be used to calculate wellhead conditions based on the reservoir model output and well geometry or adjust the well feedzones flow rates to keep the wellhead pressure below a defined minimum value.

2.3. Inverse modeling

Part of the complexity of simulating a geothermal reservoir is the variation of properties in space, making the number of parameters theoretically infinite. However, since the space is divided into defined elements, the governing equations are discretized and several volumes grouped under the same properties. Therefore, the number of parameters to be estimated is reduced. iTOUGH2 provides inverse modeling capabilities for the TOUGH2 simulator by estimating model-related parameters based on field data [18].

The input parameters such as hydrogeologic characteristics, thermal properties, initial, boundary conditions and other aspects of the model can by parameterized. The parameters $\boldsymbol{p}$ are defined as TOUGH2 input parameters and a m number of calibration points coming from observable variables on different measurement locations and calibration times specified on the vector $\boldsymbol{z^*}$ while $\boldsymbol{z}$ contains the model output values. The corresponding difference is denoted by $\boldsymbol{r}$:

$$\boldsymbol{r} = \boldsymbol{z^*} - \boldsymbol{z(p)} \tag{2.27}$$

Assuming uncorrelated and normally distributed random variables with zero mean, the residual is weighted using the inverse of the measurement covariance matrix C_{zz}.

$$C_{zz} = \begin{bmatrix} \sigma_{z_1}^2 & 0 & 0 & 0 & \ldots & 0 \\ 0 & \sigma_{z_i}^2 & 0 & 0 & \ldots & 0 \\ 0 & 0 & \sigma_{z_n}^2 & 0 & \ldots & 0 \\ 0 & 0 & 0 & \sigma_{z_j}^2 & \ldots & 0 \\ \vdots & \vdots & \vdots & \vdots & \ddots & \vdots \\ 0 & 0 & 0 & 0 & \ldots & \sigma_{z_m}^2 \end{bmatrix} \tag{2.28}$$

Each element on the diagonal represents the measurement of error of the corresponding z^* observation. The misfit between the model output and measuring data is compared using a weighted least-square, called objective function S. The objective function is defined as the sum of the square residuals, weighted by the inverse of the variances:

$$S = \sum_{i=1}^{m} \frac{r_i^2}{\sigma_{z_i}^2} \tag{2.29}$$

The minimization algorithm reduces the function S until a certain convergence criterion is achieved, either a number of iterations, number of forward runs, a certain objective function value, among other criteria. For this study the Levenberg-Marquart algorithm is selected. Since S is an n-dimensional parameter space function (Figure 2.2) the algorithm could find a local minima. Thus, in this study, multiple inversions are performed at different model stages in order to recognize the most sensitive parameters and minimize the objective function.
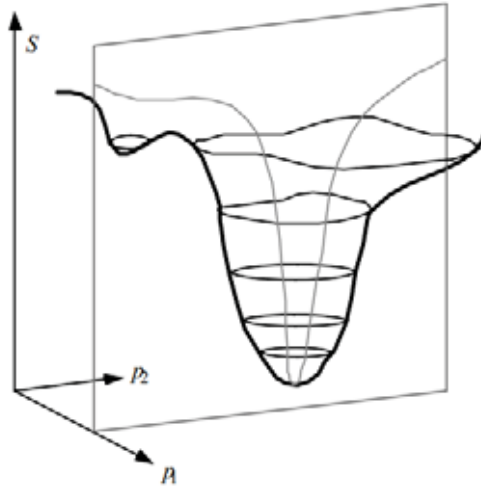
Figure 2.2: Objective function topography for a two-dimensional parameter space, from [18].

3. Berlin Geothermal Field

The Berlin Geothermal Field is located 110 km east of San Salvador (Figure 3.1), it operates as based load for the national grid and it account for the 14.75% generation of the total generation for the country in 2021 [60]. The first geoscientific study was carried out in 1953, and the first deep exploratory well was drilled in 1968 under the United Nations Development Programme and the National Electricity Company, Comisión Ejecutiva Hidroeléctrica del Río Lempa, auspice. Electricity generation started in 1992 with two backpressure units of 5 MW. In 1999 the backpressure units were decommissioned and two 27.5 MW condensing units (Unit 1 and 2) type went online. After a drilling campaign in four well pads and the encounter of steamcap, in 2008 a 44 MW condensing unit and a 9.2 MW binary unit were commissioned (Unit 3 and 4). Currently, the field has a total installed capacity of 109.2 MW with a total mass flow rate extraction of 860 kg/s. Since exploration started 45 wells have being drilled , ranging in depths from 750 to 3500 m, including 15 producers, 20 injectors, and one monitoring well. The rest are either on standby or abandoned as shown on Figure 3.2 [40, 26, 10].

Figure 3.1: Berlin Geothermal Field location, red square represents the field concession.

11
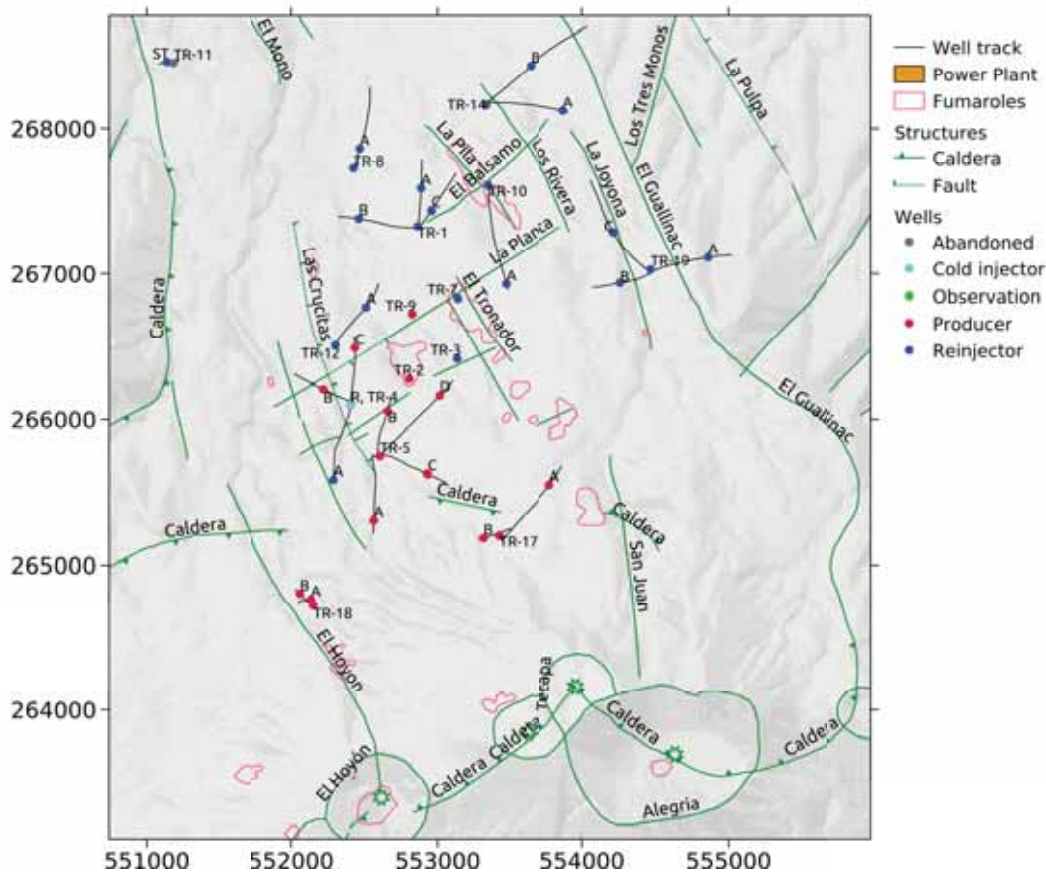
Figure 3.2: Well distribution, faults and fractures at BGF.

3.1. Geological framework

Berlin Geothermal Field is located at the northern flank of the Berlin-Tecapa Quaternary volcanic complex. The tectonic activities started 1.4 Ma and the final event presented was the phreatic explosion of El Hoyon 700 years ago. The activity has changed between effusive and explosive events with andesitic-basaltic composition. Dikes are unevenly distributed, found mainly in the northern part. The origin of the main structures is attributed to the oblique subduction of the Cocos plate under the Caribbean plate at a rate of 10 mm/y (Figure 3.3), forming a tectonic graben trending E-W on the region. The complex seems to be located on the intersection between the regional northwest-trending fault system and the southern margin of the E-W trending fault system [57, 2, 14, 19].

The fault system NW-SE is associated with the most recent activities and allows the ascents of fluids from the deep reservoir as most of the hydrothermal manifestations are found within this structure [4]. The subsurface geology has been described with four units based on the lithology obtained from all the wells drilled on the area
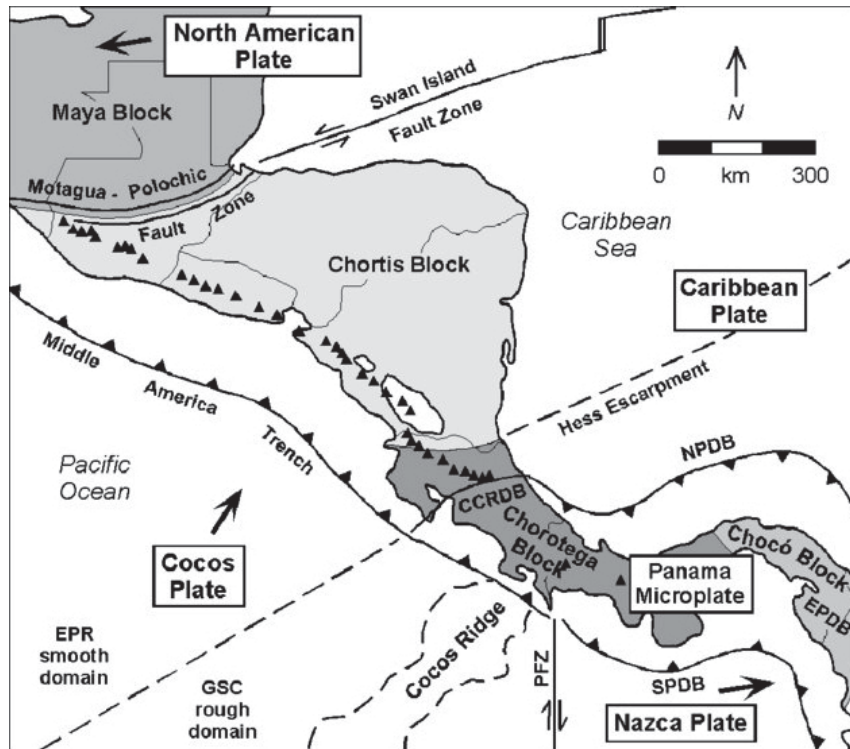
Figure 3.3: Central America Geodynamics, arrows represent plate direction relative to the Caribbean plate, from [37].

using macroscopic analysis and petrographic data. A summary of the stratigraphy is presented on the Table 3.1.

Table 3.1: BGF Stratigraphy, adapted from [4] and [26].

Unit	Lithology	Description	Thickness [m]
I	Andesite - basaltic andesite, secuences of fine tuffs and lithic tuff	Pyroclastic deposits	600 - 800
II	Ignimbrite deposits intercalated with scoria and thin layers of andesite lavas	Intermediate aquifer	570 - 850
III	Cineritic tuff with Plagioclase with layers of andesitic lava flow	Caprock	100 - 345
IV	Andesite, andesitic brecias, basaltic andesite with lithic tuff, abundant presence of dykes, granodiorite and granite	Geothermal reservoir	370 - 920

The southern and northern region of the field have a different alteration mineral distribution, mainly changing by the depth at which the minerals are found. Based

13

on the rock formation and the alteration temperature of secondary minerals, five mineralogical facies are defined for the BGF [4, 46, 26, 52].

- *Argillitic*: clay minerals, indicates temperatures ranging from 50 to 150 °C , at 500 Metersabovethesealevel(masl) on the south and 150 masl on the north.
- *Argillitic-phylitic*: clay minerals type chloritic, suggests temperatures between 150 to 180 °C, at the elevation of 100 masl on the south and 100 mbsl on the north.
- *Phyllitic*: clorite minerals and decrease of clays, indicates temperatures from 200 to 230 °C, found at 400 mbsl on the south and 700 mbsl on the north and average thickness of 600 m.
- *Phyllitic-profylitic*: ranging temperatures from 230 to 260 °C, characterize by chlorite group (penninite), found at 950 mbsl on the south and 1200 mbsl on the north.
- *Propylitic*: stabilized temperatures are between 260 and 300 °C, represents the complete development of epidote, the lower limit has not been identified

3.2. Geophysical studies

Several surveys have been carried out on the field since 1977, including magnetotelluric , electric and gravimetric. A low resistivity attribute to a shallow horizontal conductor. It consists of a few ohm-m, and thickness of some thousands of meters. However, it thins and deepens towards the north of the production zone. The $30\,\Omega\,m$ mark is seen as the beginning of the propylitic alteration facies where the geothermal reservoir is hosted. The western side of the production area presents a deep vertical conductor with resistivity ranging between 15 to $20\,\Omega\,m$ related with the edges of the system [2, 36].

DC resistivity surveys suggest the outflow zone is located on the NNW fissure swarm, the correspondence between high resistivity surface values and fresh cold rocks outside of the geothermal field, and a high correlation between the high resistivity core and the mineral alteration [52].

Gravimetry residual anomaly map presents transitions from positive to negative gradients on the east by Las Crucitas and on the west by El Guanillac faults due to the combined effect of differences in the density of the numerous extrusion and pyroclastic flows. On the southern side, the presence of a negative anomaly is related to steam or lower density material filling the subsurface structures [51].

Seismic monitoring shows a reduction of epicenters below 6000 mbsl which can pro-

vide possible delineation of a ductile zone related with the geothermal field heat source as shown in Figure 3.4 [48, 47].
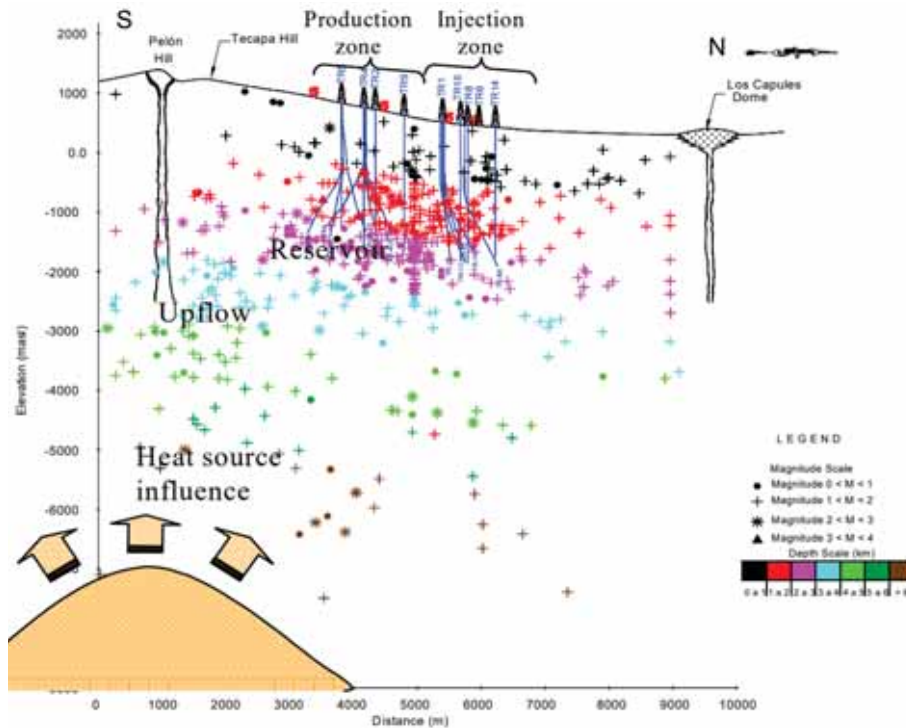
Figure 3.4: Hypocentres location from 1996 to 2003 on the $553\,000\,\text{m}$ *East mark, notice the reduction in events below* $6000\,\text{mbsl}$, *from [47].*

3.3. Geochemistry

Chloride content in the geothermal field ranges from 3200 to $5500\,\text{mg/l}$ from the south-western to the north-eastern area. The meteoric origin of the liquid phase has been proven to feed the fumaroles and wells at the geothermal field. The isotopes analysis locates the recharge zone at around $1305\,\text{masl}$. The gas content (NH_3, B and H_2) indicates the heat source is located on the south of the field, beneath the Tecapa volcano. Discharge waters are sodium-chloride type, ranging from 3000 to $6000\,\text{ppm}$ for chloride content, pH from 6.1 to 7.5, TDS from 7000 to 20000 and gas steam ratios from 0.1 to 0.3 % [2, 39, 13, 26].

3.4. Hydrogeology

Based on chemical measurements, logs while drilling, vertical electrical soundings and Total Loss Circulation (TLC), two main thermal aquifers have been identified:

- *Shallow aquifer*: between the elevations of 200 masl and 300 mbsl, present temperatures on the interval from 90 to 100 °C, and found only the wells on the NE side of the field.
- *Intermediate aquifer*: between 250 masl and 50 mbsl, it ranges temperatures between 150 to 200 °C. It is found on most of the wells on the field.
- *Deep hot saline aquifer*: it presents temperatures from 300 to 250 °C from south to north. For the south area it is found between -900 to 1200 mbsl while on the north between 1300 to 1500 mbsl [36, 4].

3.5. Conceptual Model

The conceptual model from BGF has been updated throughout the years as new wells are drilled, new surveys are carried out, and monitoring during production continues. The geothermal reservoir is characterized by resistivity above $30\,\Omega - \mathrm{m}$, prophylitic facie, and temperatures ranging 240 - 300 °C. The change in permeability from the north and south side of the field is distinguishable from the anomalies in gravity surveys. The heat source is located underneath the Berlin-Tecapa volcanic complex related to a magmatic chamber. The flow path moves primarily from the South to North-West through the graben structures.

The flow recharge is meteoric and the outflow of the systems has not been confirmed yet. Nevertheless, it is associated with hot springs located in the north side of the field. The reservoir seems to be delimited by the lineaments trending NW-SE by El Guanillac, El Hoyon, Las Crucitas, and Tecapa, NE-SW by La Planta, and by the volcanic belt on the south [2]. The main features of the current understanding of the field are portrait in the Figure 3.5.
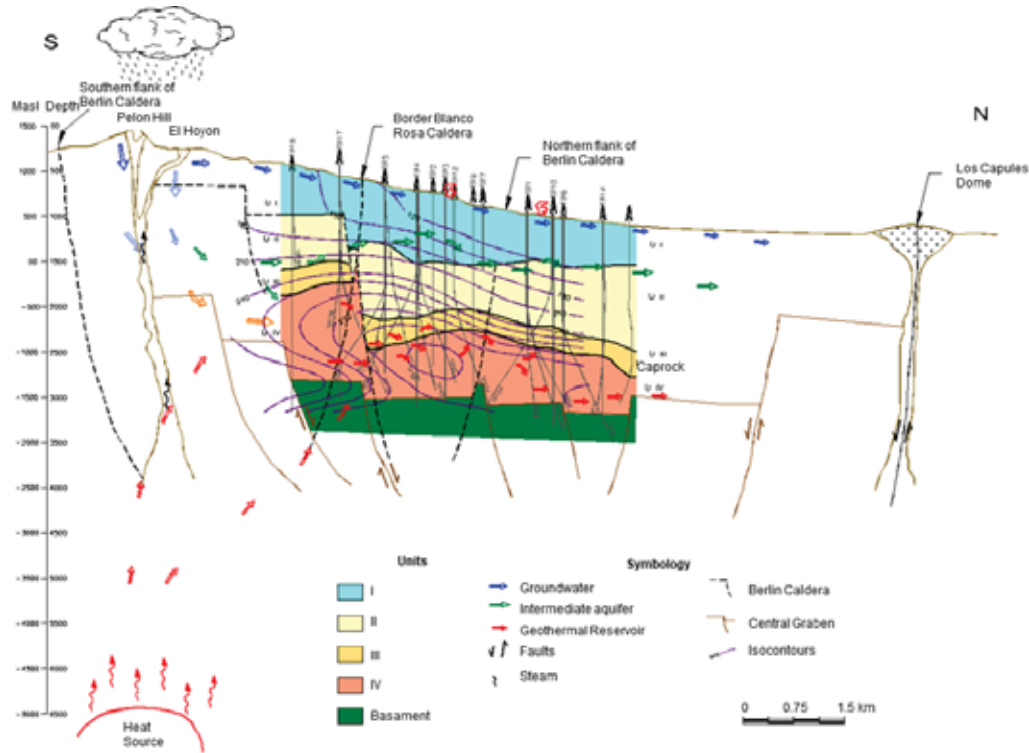
Figure 3.5: Berlin Geothermal Field conceptual model, N-S section along stratigraphy units (Table 3.1). Arrows represents flow pattern and gray lines well tracks, modified from [33].

3.6. Field development and reinjection management

Reinjection began during the operation of the backpressure units in 1992. TR-9 was used for disposing of brine and TR-1 for cold waters; eventually TR-8 and TR-14 were drilled and included in the generation process [9]. A second expansion came after a drilling campaign for Units 1 and 2, including the eleven new wells on well pads TR-1, TR-8, TR-11, TR-12, and TR-14. A pump station was installed on the well pad TR-1 to assure the injection capacity of the field due to the low injectivity index of wells in TR-1. For generation purposes, at this stage, well pads TR-2, TR-4, TR-5, and TR-9 feed Units 1 and 2. With the commissioning of Unit 3, new areas were explored on the northeast side of the field. Four new wells were drilled on well pad TR-19 to inject the brine from wells at well pads TR-17 and TR-18. During this campaign, the shallow steam cap was encountered on the south of the field. As shown in Figure 3.2, some injector wells are located nearby the production area. Hence, a slight cooling has been observed on the pads TR-4, TR-5, and TR-9 [49, 27, 25]. Figure 3.6 presents as one pressure drawdown time series the monitoring pressure at 0 masl from four different wells: TR-4, TR-4A, TR-3 and TR-12A, as well as the net mass flow extraction from the field. A delayed response can be seen

in the monitoring well but during 1992 to 1995 the pressure is stable. However, from 1996 to 2000 the pressure dropped about 10 bar, the same pattern is observed from 2000 to 2005 when the pressure stayed unchanged, a slight decrease every year was observed up to 2016 when the well TR-4 was used for production purposes, afterward, it was found the pressure dropped to 35 bar. This behavior is attributed to the high apparent compressibility of the two-phase conditions on the geothermal reservoir [20].
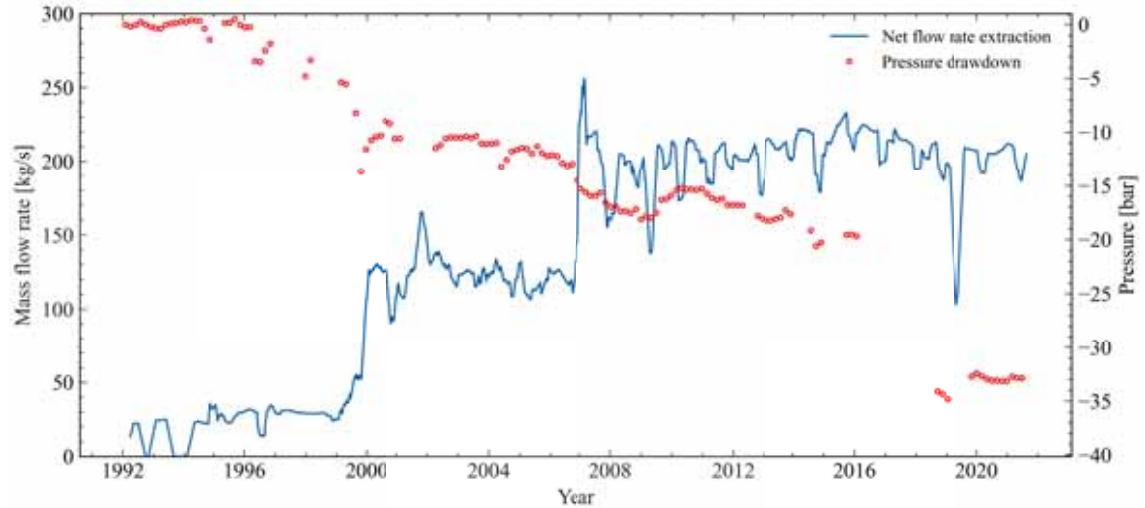
Figure 3.6: Net flow rate extraction (180 days MA) and pressure drawdown at sea level (60 days MA).

3.7. Well data

A vast number of logs have been performed on the field since the first drilling campaigns during warm-up periods, static conditions (Closed and bleeding), and dynamic conditions, acquiring down-hole measurement have yielded information for a comprehensive understanding of the formation conditions and field response. They are performed regularly by LAGEO staff at the field during Units overhauls to the wells feeding the corresponding unit. The data in this study is provided from the database GMS at LAGEO [33].

Figure 3.7a shows the temperature distribution at 1015 mbsl, where the highest temperatures are found on the well pads TR-2, TR-4, TR-5, and TR-9 and a medium temperature on the south area (TR-17 and TR-18). Nevertheless, Figure 3.7b presents higher enthalpies on wells TR-18's for a lower liquid saturated enthalpy (TR-17's). Notice the increase in flowing enthalpy on the wells in the south in late 2015, which effects are still visible in 2022. Such situation is not attribute

to any field operation; therefore, attributed to a geological event. Based on these observations, the field is divided into four areas in this study: the Center where the highest temperatures are presented, the South related with the wells encountering the steam cap, the North where the wells from the Center dispose their brine, and the North-East on which the wells from the South reinject their brine.
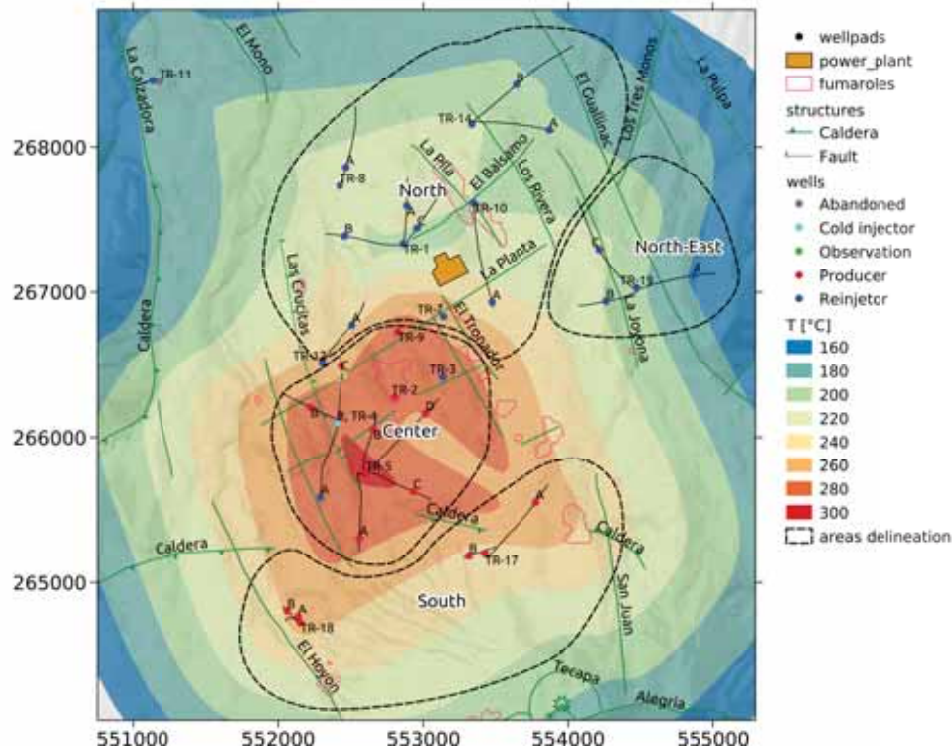
(a) Formation temperature distribution at 1015 Meters below the sea level (mbsl).
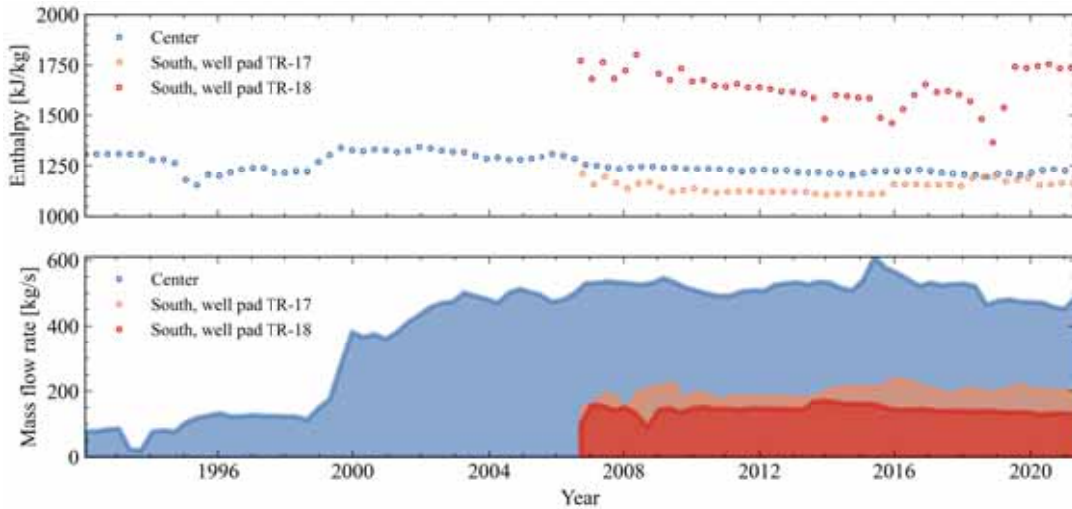
(b) Mass flow rate and flowing enthalpy from production wells on defined areas.

Figure 3.7: Temperature distribution and defined areas in this study.

3.8. Previous reservoir modeling studies

Some detailed reservoir models had been done for BFG. They were developed and based on the new findings and data availability mainly for forecasting purposes. Some of the primary modeling related conclusions are listed:

- Monterrosa (1993): covers $120\,km^2$, five layers and 152 elements. Indicated the boiling in the reservoir as a possibility for the minor drawdown observed after one year and a half of production.
- Monterrosa (1992): extends $100\,km^2$, seven layers, and 546 elements. No breakthrough was observed due to reinjection, and enthalpy excess was identified in some wells.
- ENEL (2003): includes $45\,km^2$, 18 layers, and 3757 elements. Anisotropy and one-order difference in permeability trending SE-NW was found. The geothermal reservoir boundaries correspond with resistivity anomaly.
- LAGEO (2007): consist of $196\,km^2$, 12 layers, 2280 elements. Inflow is located between Cerro El Hoyon and the TR-18 well pad. It deals with the formation of a steam cap on the southeast side of the field.

4. Numerical model

4.1. Mesh definition

The boundaries of the geothermal reservoir define the mesh extension, it is extended around $3\,\mathrm{km}$ in all directions from the well field, to provide stable boundary conditions to the model and far enough to minimize its influence in the mass extraction and related phenomenon occurring at the well field. The far field is delimited by transition from 7 to $10\,\mathrm{ohm-m}$ at the magnetotelluric data at $400\,\mathrm{mbsl}$.

Since the fault structures on the southern side of the field trend NNO-SSE, the mesh is rotated $26.7°$ to align the elements in the main flow direction to reduce as far as possible the number of elements necessary to define the flow pathways. Starting on the coordinate 551000m E, 259000m N, it extends $9.5\mathrm{x}13\,\mathrm{km}^2$ in the rotated axes. The thickness is defined as $3.39\,\mathrm{km}$ depth ranging between $500\,\mathrm{mbsl}$ and $2890\,\mathrm{mbsl}$. The farfield contains square elements of 1x1 km, while the wellfield is populated with honeycomb shape elements every $175\,\mathrm{m}$. However, on the wellfield, no honeycomb element is placed closer than $50\,\mathrm{m}$ from a well. The wellfield elements are significantly smaller than the farfield to closely monitor the thermodynamic variables due to the high gradients in temperature and pressure expected during the production stage. Along the El Beneficio, Las Crucitas, San José, and La Planta faults, several elements placed every 25m, and two offset rows parallel on each direction are defined to set a preference path along these structures. To properly define each well condition, 10 points are radially distributed around each well projected feedzone. A total of 9 Lloyds iterations are executed to optimize the mesh.

The mesh consists of 21 layers, 65750 elements and 257616 connections. The thickness of each layer varies depending on the geothermal reservoir features. As a general rule, the layers above the caprock and nearby the basement are coarse. A general view of the mesh is presented in Figure 4.1. The mesh was generated based on the Voronoi tessalation method using AMESH [24], the input file was prepared using T2GEORES [30] and the rock assignation Steinar [16].
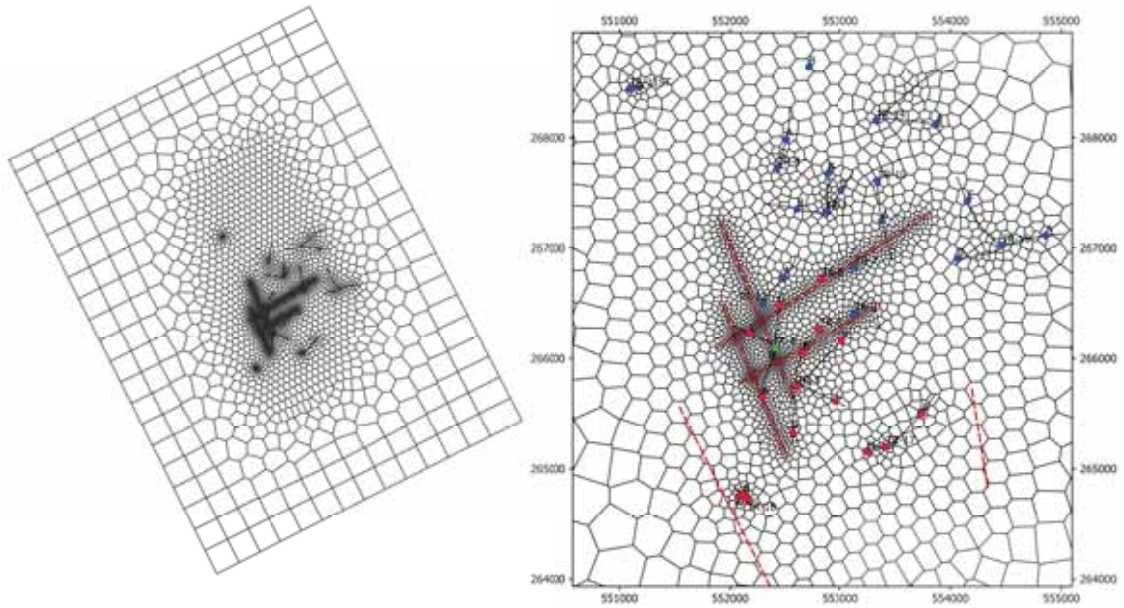
Figure 4.1: (a)Mesh layout of BGF (b) Mesh on well field, blue dots represents injector wells, red producers and green monitors.

4.1.1. Vertical structure

The stratigraphy and feedzones are the primary input variables to consider the number of layers and their thickness. The stratigraphy units I to IV are encountered in most of the wells. For modeling purposes, the different units are intended to be used as defined by Monterrosa [40]. The caprock delineated by the Unit III is shallower on the south, around the wellpads TR-17 and TR-18 and it deepens towards the north. Whereas the Unit II, is thinner in the south, on which the shallow aquifer resides. The convective trends in temperature are found mainly on the SE side of the field. Hence the permeability values decrease one order of magnitude from SE to NW [2]. A total of 23 rocktypes are defined. The layer distribution and thickness are shown in Figure 4.2.
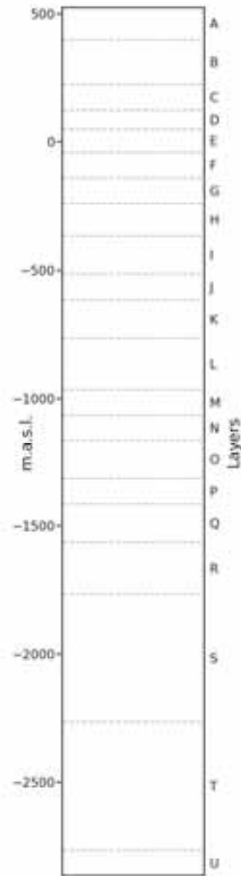
Figure 4.2: Layers distribution.

4.2. Initial and boundary conditions

Initial conditions for the model correspond to a hydrostatic column of saturated water. However, based on the water level presented at the formation conditions, the column starts 200m below the top layer. Hence, the pressure on the first 200 m is nearly isobaric. An initial temperature gradient of 60 °C/km is used; since the top of the mesh is located at 500 masl, the temperature top layer is fixed at 50 °C and a pressure of 1 bar. There are two types of boundary conditions on the model: Dirichlet and Neumann. The first refers to constant conditions, and the second to specified gradients along a given boundary. The top (A) and bottom layer (U), as well as the farfield, keep their P&T conditions throughout the simulation, accounting for 12570 elements; some elements on layer T (second last from the top) contain a constant mass inflow of 12.85 kg/s per element at defined enthalpy of 1280 kJ/kg, individual heat inflows of 290 kW and the fumaroles are represented using the deliverability approach on different layers. The boundary conditions are represented in the Figure 4.3.
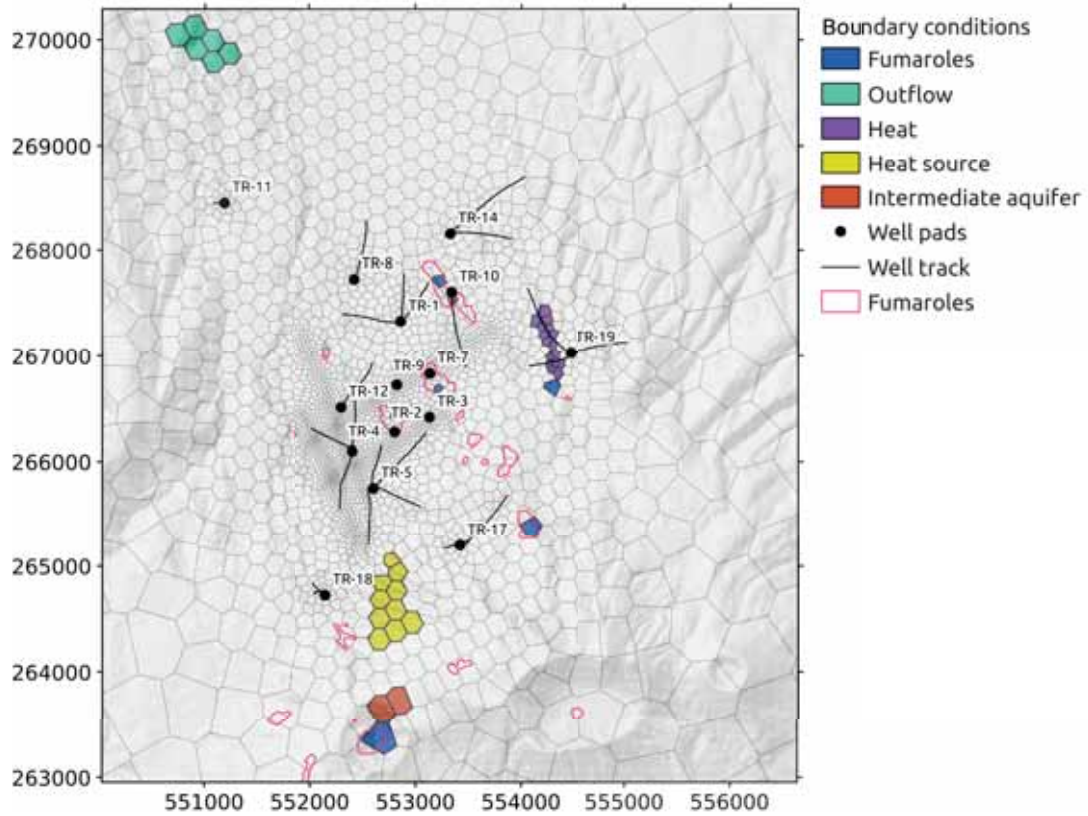
Figure 4.3: Boundary conditions layout. Fumaroles, Outflow and Intermediate aquifer are located at upper layers while Heat Source and Heat at the second last layer from the top.

For the top and bottom layer the P&T are established based on the formation conditions:

- At the uppermost layer, the distribution is made assigning 50 °C and 1 bar to the farfield elements, extracting the corresponding conditions at the mid-top layer elevation and remapping the other elements conditions on the nearfield by a linear distribution using the griddata function the SciPy package [61].

- For the lowermost layer, the initial pressure gradient for each well is extended, and the corresponding pressure for 2890 mbsl is assigned to the elements within 150m distance. The deepest temperature value from the formation conditions is assigned to the deepest element within a radio of 150 m, the farfield is set at 253 °C, the temperature for the elements on the nearfield is found by linear interpolation.

Feedzones

The feedzones depth are selected based on the drilling reports and P&T loggings, while the initial flow distribution on injectivity test during completion. During the calibration process, the mass flow distribution is adjusted to comply with the wellbore simulator constraints. Each feedzones is defined as a MASS source type in TOUGH2 with a time dependent mass flow rate. The feedzones are ideally placed at the middle of the nearest layer. Nevertheless, due to proximity and model discretization, some feedzones were either moved to the nearest layer or merged into a single layer. A 3D representation from the well tracks and feed is shown in Figure 4.4.
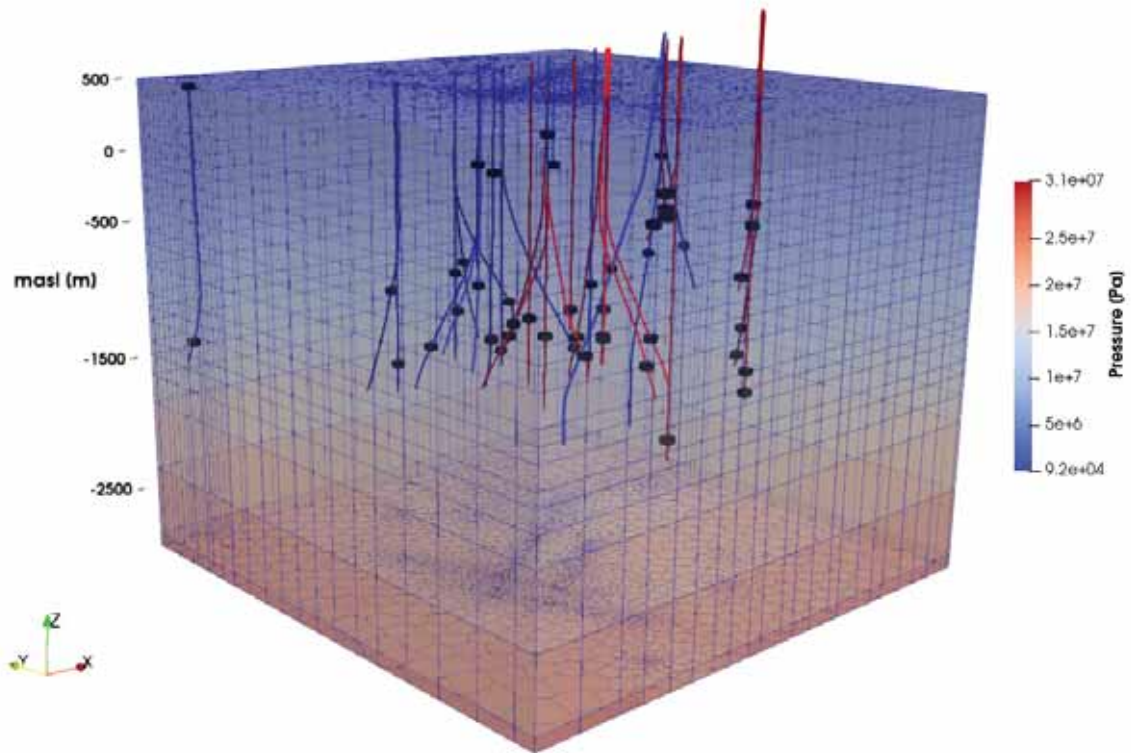
Figure 4.4: Initial pressure distribution at the well field, black boxes represent identified feedzones. Blue well tracks are injector wells and red tracks production wells, initial pressure distribution is represented within the grid.

4.3. Wellbore definition

Each well geometry is specified at the FLOWELL section. The wells are divided into several segments from the deepest identified feedzone to wellhead considering the trajectory of directionally drilled wells. Figure 4.5 outlines the definition for well TR-5A; the measured depth is presented on the right side and the red box indicates the feedzone.
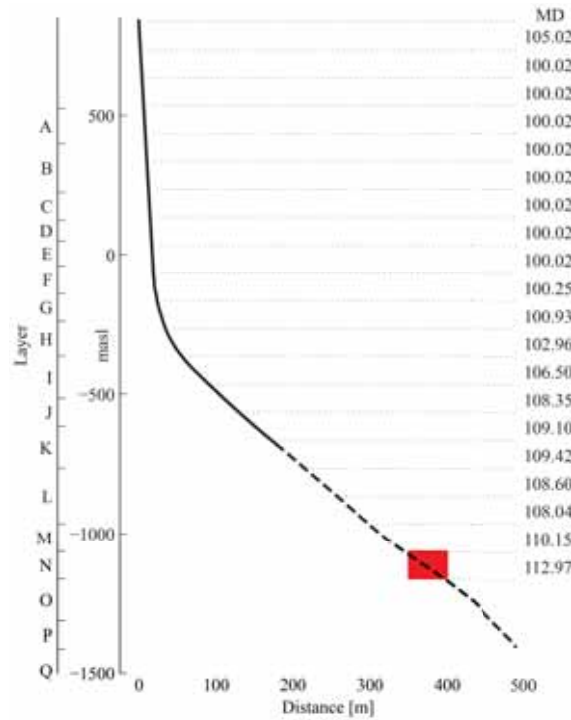
Figure 4.5: TR-5A wellbore definition, red box stands for the feedzone location, measured depth in meters is shown on the right side, the solid line represents the production pipe and dashed line the liner.

Based on the many tests presented by Guðmundsdóttir (2012) using FLOWELL for calibrating geothermal wells; the Swamee and Jain correlation [56] for the friction factor, Beattie [5] for the correlation factor, and Rouhani and Axelsson [50] relation for the void fraction are selected .

4.4. Rock properties and permeability distribution

The initial hydrological properties distribution is assigned layer by layer based on the conceptual model and each well stratigraphy. Therefore, faults, barriers, and

system boundaries are represented by different petrophysical parameters. However, during the calibration process, especially during the production stage, the rock type distribution is altered, and some new rock types are included.

The permeability distribution is performed using Steinar [16] and a base map with the main geological features from the field. Most of the rock properties are homogeneous; the density is established as $2650\,\text{kg/m}^3$, specific heat is $1000\,\text{J/kg°C}$, heat conductivity is $2.5\,\text{W/m°C}$ and porosity $10\,\%$. Nevertheless, for the geothermal reservoir related rocks, the porosity is set at $7\,\%$. Moreover, the permeability is anisotropic for most of the rocks; as a general rule, the horizontal values are smaller than the vertical component.

The top layer is assigned to the rock type SURFA; the second top layer mainly consists of the material RESU1. Underneath, distributed among various layers, RESU2 holds the shallow aquifer. One of the lowest permeabilities in the system is assigned to the caprock, which is spread based on the U3 occurrence and represented by the RESU3 rock type; it is shallow on the south and deeper on the north. Below the caprock, the main geothermal reservoir material is RESU4. However, from the heat source location to the well pads TR-5 and TR-4, a higher vertical permeability is assigned to U4UPF to develop higher temperatures at the center of the field, maintaining the heat source location according to the conceptual model. Finally, in order to avoid any inflow or recharge from the bottom layer of the model, a uniform low permeability is assigned; it is represented by the material named BASEM.

The heterogeneity of the model is illustrated by explicitly representing the faults, Las Crucitas, El Beneficio, San José, and La Planta on the mesh and permeability distribution, both assigned to materials with higher permeability than the rock type RESU4 to drive the temperature front to the NNW at the center of the field and ENE towards the reinjection zone. A horizontal cross-section on layer M and vertical cross-section A-A' are presented in Figure 4.6.
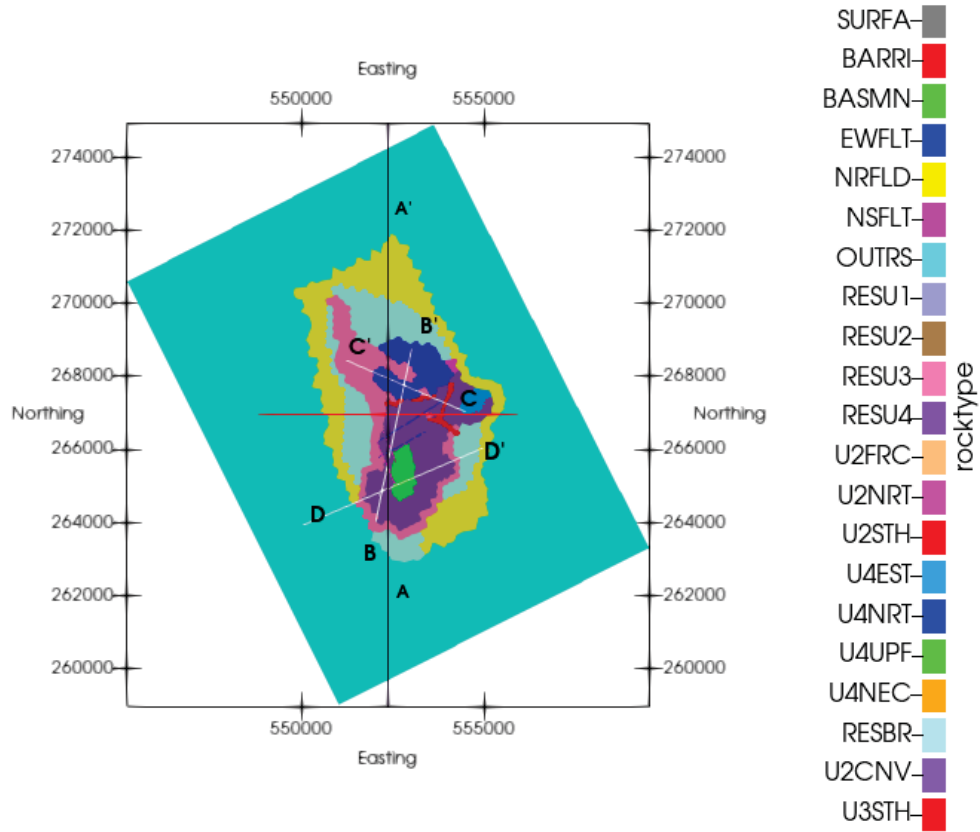
(a) Rock distribution at 1070 masl.
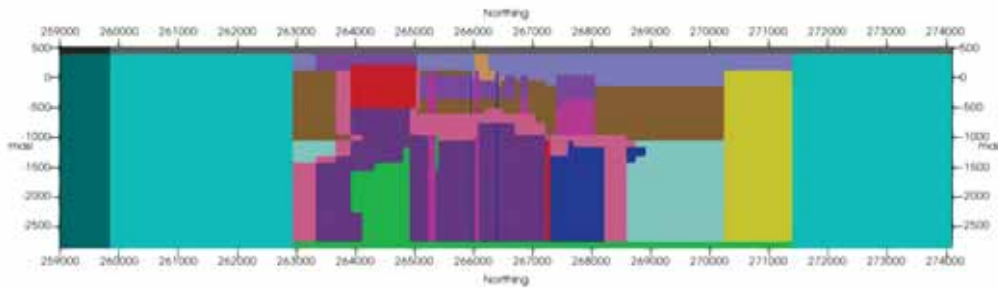
(b) Vertical cross section A-A'.

Figure 4.6: Rocktype distribution.

4.5. Model setup generalities

This section describes various aspects regarding the settings used during the simulation:

- Although the fluid chemistry shows the presence of gases and minerals, the wellbore simulator considers the fluid to be pure water. Hence, the equation of state 1 (EOS1) is selected.

- Due to its agreement with field and experimental data [21, 28], the Corey curve [11] was selected as a relative permeability function. The steam (S_gr) and water(S_lr) irreducible saturation were set at 0.03 and 0.4 respectively as shown in the Figure 4.7.

- A similar approach as described by Bjornsson [6] was implemented; the iTOUGH2 STEADY-STATE command was used to reach a steady-state when the time step exceeded 10.000 y to ensure the continuation to the production state in one single runtime.

- Among other model parameters, the step reduction when convergence fails was set to 3.5, the linear solver the Lanczos-type preconditioned bi-conjugate gradient solver [34] and a linear function for the capillary pressure was selected.
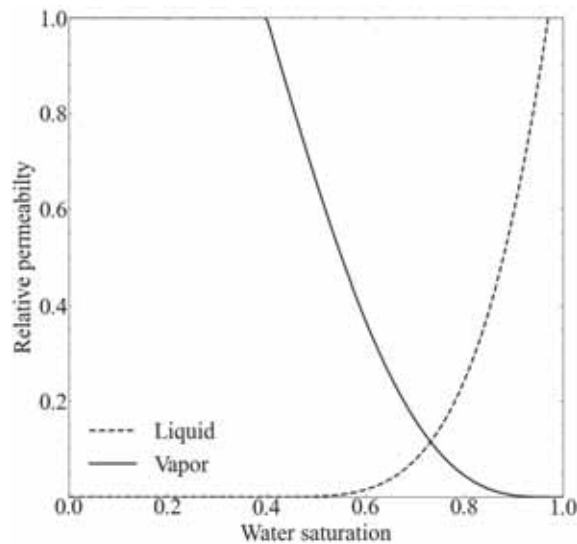
Figure 4.7: Relative permeability function.

4.6. Data processing and calibration

This section describes the data processing for each subset of information required for calibration.

4.6.1. **Formation conditions**

Several logs are provided for each well; some were collected after a long warm-up period after drilling was finished. Hence, for such cases, the P&T measurements are directly defined as formation conditions [55]. The recorded measurements are listed on the OBSERVATION section on the iTOUGH2 input file. Based on the logs compilation two vertical cross-section are presented in the Figure 4.8 sections are refereed to the Figure 4.6. Section B-B' reveals the upflow zone underneath the well pads TR-4 and TR-5 and a relatively shallow high temperature associated with the southern wells. Section C-C' shows the temperature deepening on the north and the cold temperature on the northwest side of the field.
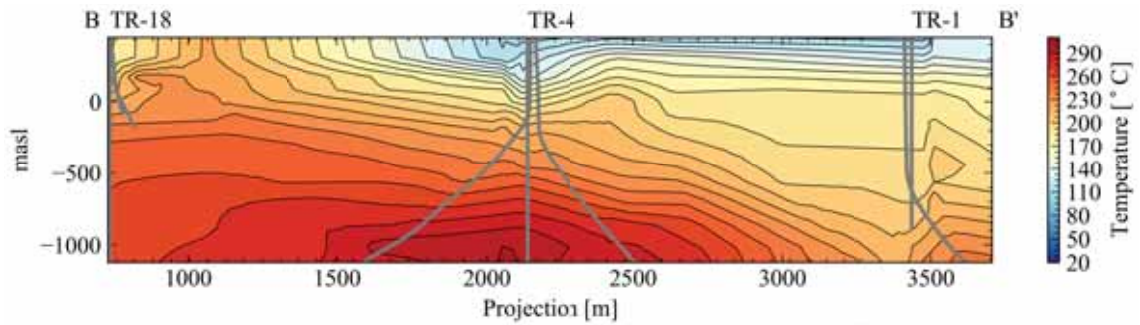
(a) Section B-B' from Figure 4.6.
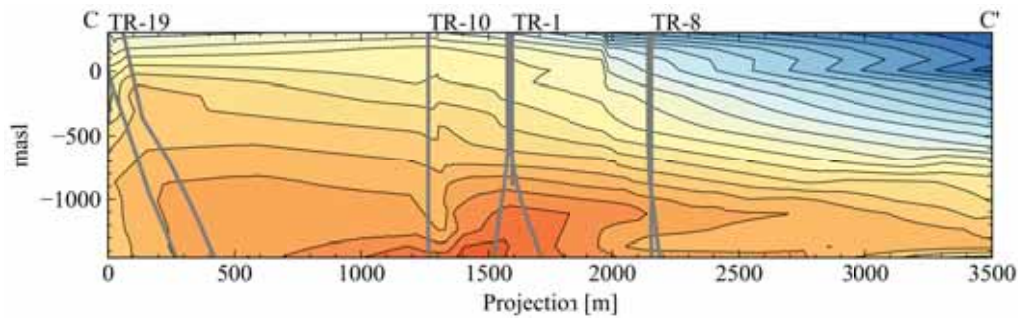
(b) Section C-C' from Figure 4.6.

Figure 4.8: Vertical sections from down-hole measurements, linear interpolation is performed between the well tracks

4.6.2. **Flow rate and flowing enthalpy**

Each well in the model is provided a time series of total mass flow rate and flowing enthalpy measured at the wellhead. The time series for the mass flow rate is directly used at the GENER section for all the wells. To reduce the number of time steps, the model runtime and portrait a representative mass flow rate, two preprocessing approaches are considered; the first one performs an average between every 15th of

the month, and the second finds the slope between every 15th of the month for a time vs. the cumulative sum of mass. A schematic representation of both remapping methods is presented in Figure 4.9. Both approaches have similar averaged differences and standard deviations compared to the original data, the first approach is employed in this study, Figure 4.10 serves as an example of the remapping results.
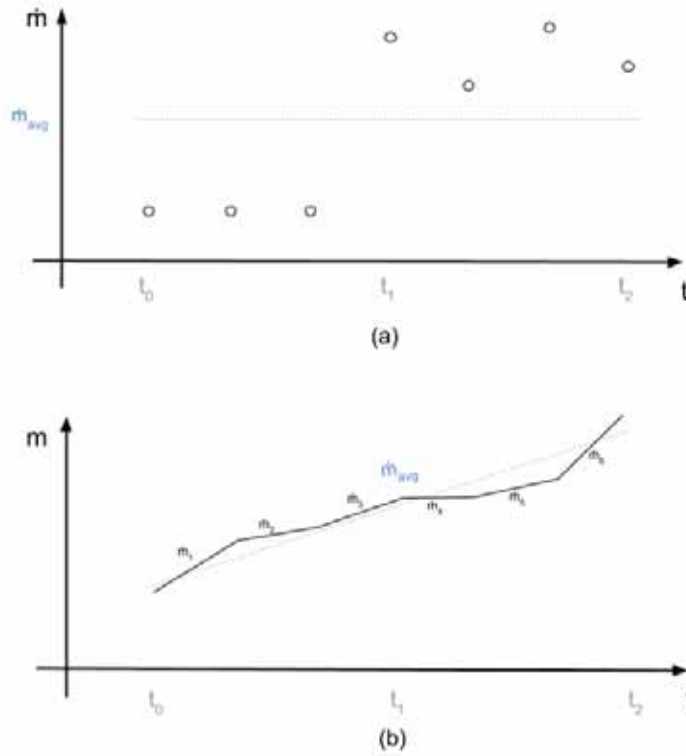
Figure 4.9: Mass flow rate remapping approaches, (a) sub-interval average method (b) sub-interval cumulative method.

The flowing enthalpy is used to calibrate the model during the production stage; it contributes to the objective function during the inverse modeling by assigning weight to the difference between the measurements and calculated value to the corresponding mass sources. Since the mid day between every moth is different, the flowing enthalpy time-series is listed at the corresponding day as the mass flow rate is defined.
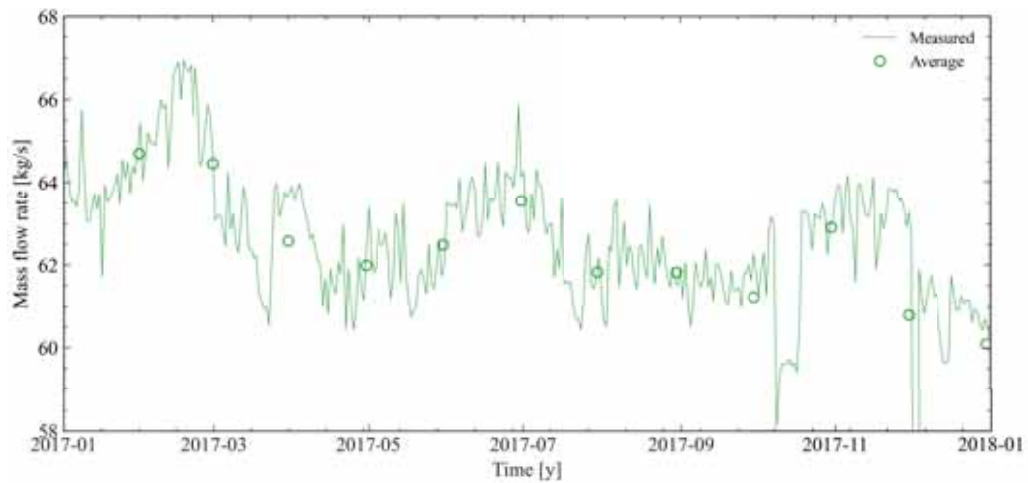
Figure 4.10: Measured and average flow rate from well TR-17.

4.6.3. Pressure drawdown

The logging campaigns provide P&T on static conditions. By evaluating the permeable zones of each well and the available data, a time series for pressure is constructed. Hence, incorporated into the calibration dataset, an example is shown in Figure 4.11. However, the drawdown is listed in the inverse file observation section instead of the absolute pressure values.
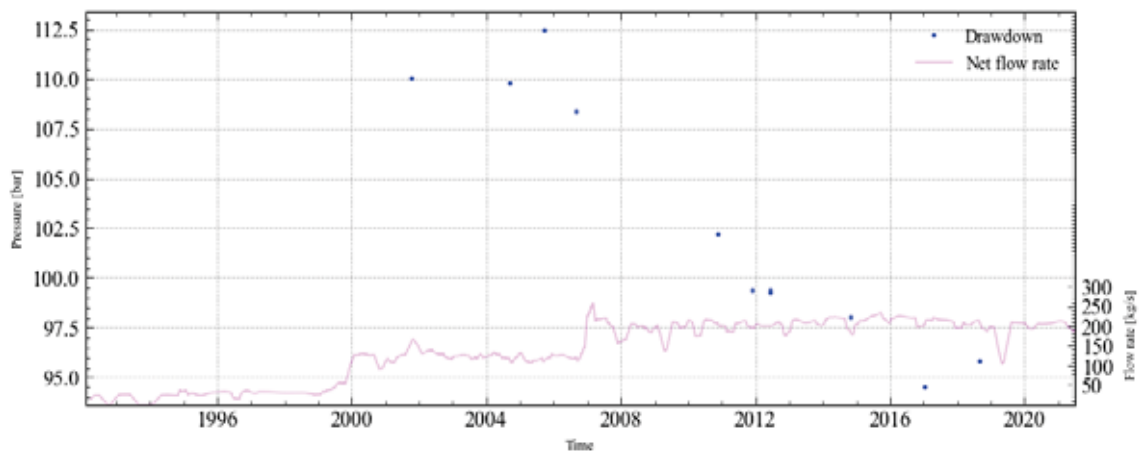
Figure 4.11: Pressure drawdown at 1015 mbsl *on well TR-5C.*

As for the flowing enthalpy, a time series is generated for the wellhead pressure at the same datetime as the mass flow rate. An example is shown in Figure 4.12.
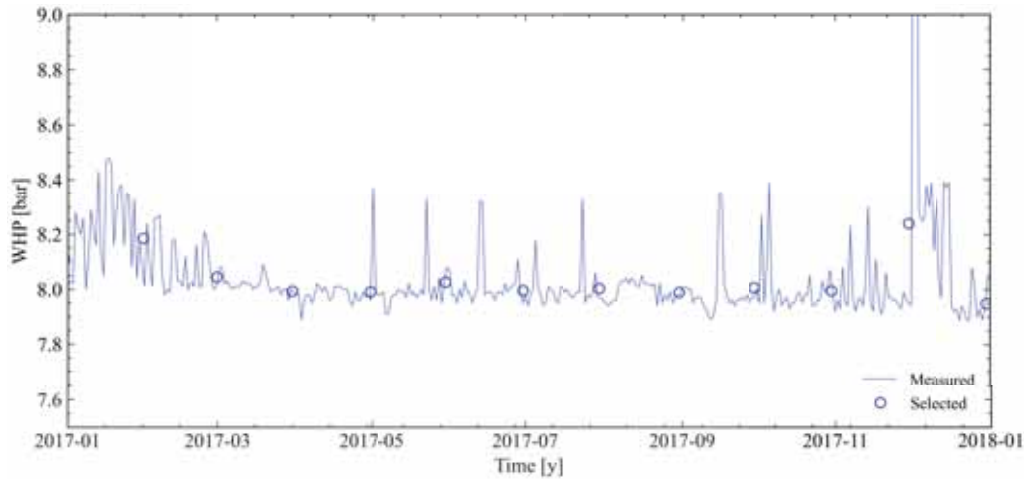
Figure 4.12: Measured and selected well head pressure from well TR-17.

4.7. Calibration process

The calibration process is divided into two main steps:

- Trial and error consists of manually adjusting the main hydrological parameters values and distribution until a good match between observed and calculated data is achieved.

- Inversion: uses the trial and error results from the previous step, to perform an automatic parameter estimation using iTOUGH2 based on the OBSERVATION section described in the section 4.6

Figure 4.13 portraits the general procedure followed during the calibration process. The trial and error stage is time-consuming, and depends on the model development stage. During this stage, the MOP 32 [17] was extensively used for debugging the producing wells when due to low permeability, the pressure reaches low values or in injector wells when due to high permeability, the pressure exceeds a predefined pressure value. Several inversions were executed in parallel at different stages of the model using 3 to 10 iterations of the Levenberg-Maquardt [35] optimization algorithm. The runtime during inversion could vary from 1 to 5 days. Moreover, after each run, the post-processing steps and debugging add extra time to the process. The calibration stops after the minimization algorithm obtains no significant improvement. The input file preparation and TOUGH2 output postprocessing are performed using the Python library T2GEORES, which the author maintains and has enhanced during the development of this study.
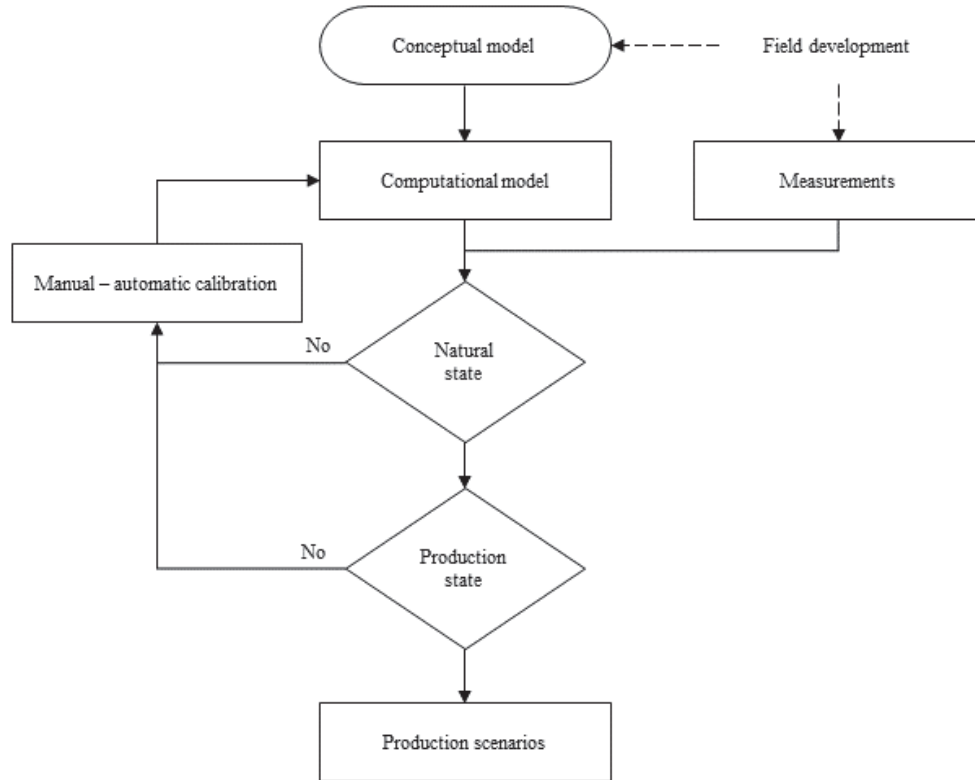
Figure 4.13: General model development approach.

4.8. Production scenarios

Four different production scenarios are explored once the model is calibrated.

- Scenario 1: no load , consist in shutting down all the production and reinjection wells in the year 2024. It tries to estimate the necessary time for the field to recover its initial conditions.

- Scenario 2: constant number of wells, estimates the flow reducing due to increase in pressure drawdown keeping the number current wells on the field.

- Scenario 3: constant power generation for 30 y, maintaining the mass flow rates at the same level, introducing make-up wells when needed.

- Scenario 4: same make-up wells as in scenario 3 with cold reinjection, estimates the cold front expansion due to the reduction in temperature in well pads TR-1 and TR-10 after installing a secondary binary plant at the field.

5. Results

This chapter presents the outcome from modeling, divided into three sections as referred in Figure 4.13: Natural state, Production state, and Production scenarios.

5.1. Natural state

The natural state refers to the undisturbed state prior to the mass extraction. P&T from the middle of each block assigned to wells in the model are extracted and compared to measurements before the transient period starts. Excluding the top and bottom layer where the thermodynamic conditions are fixed, Figure 5.1 presents a scatter plot with the results. Moreover, Figure 5.2 presents the histogram from the differences between measurements and the model, which shows a normal distribution, implying that there is no systematic error in the model. Overall, the downhole measurements and calculated values are in good agreement, having a correlation factor of 0.86 for temperature and 0.98 for pressure. However, two main observations are noticeable from the Figure 5.1a: the temperature is overestimated for some wells where the temperature is above 260 °C and around 175 °C (Shallow aquifer and caprock) the model estimates a wide range of values (125 to 200 °C). Furthermore, Figure 5.1b presents several points over discrete calculated pressures; this behavior is observed due to small changes in pressure within the same layer. Therefore, there is still room for improving the natural state calibration.

The logs are presented in the Appendix A.1. In general, the model yields better results in the Center and South areas of the field and is less satisfactory towards the North-East (TR-19's). Figure 5.3 shows an example of a production well match between the model and measurements, above previous results during the calibration process.

Figure 5.4 provides the temperature distribution over section A-A' in the rocks associated with the geothermal reservoir. The southern temperatures contour lines are vertical due to the high steam saturation in the area. The hottest contour lines are displayed around the well pads TR-5 and TR-4; towards the north, a temperature reversal is observed caused by a convection cell.
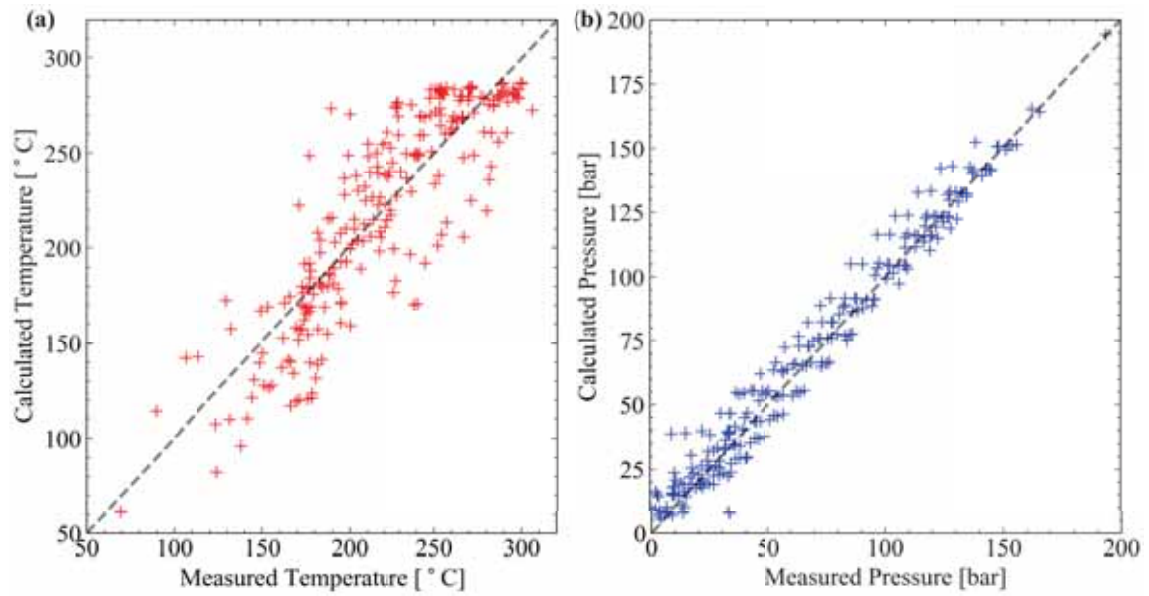
Figure 5.1: At $t = 0$ s, (a) Comparison between measured and calculated temperatures, (b) Comparison between measured and calculated pressures.
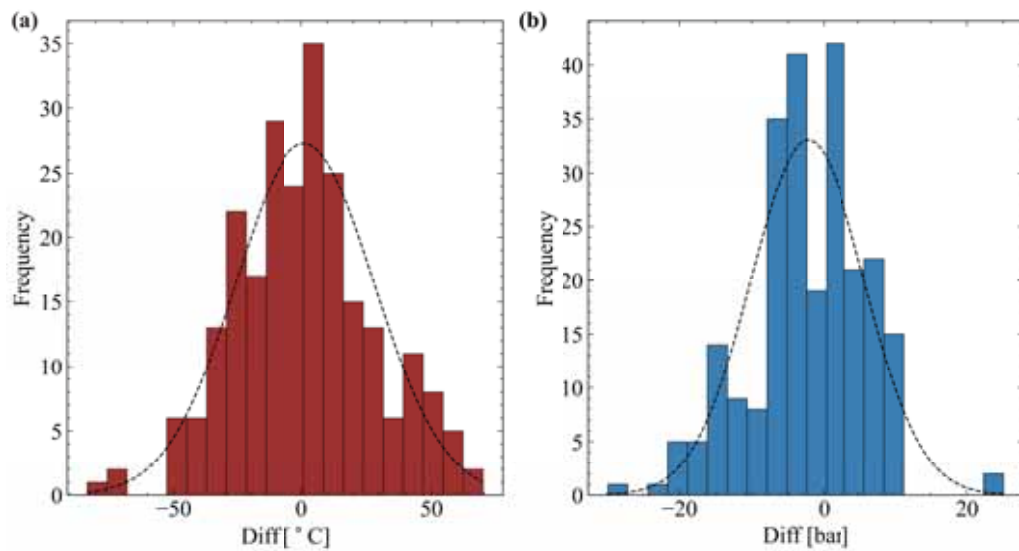
Figure 5.2: Difference distribution between temperature (a) and pressure (b), at $t = 0$ s.
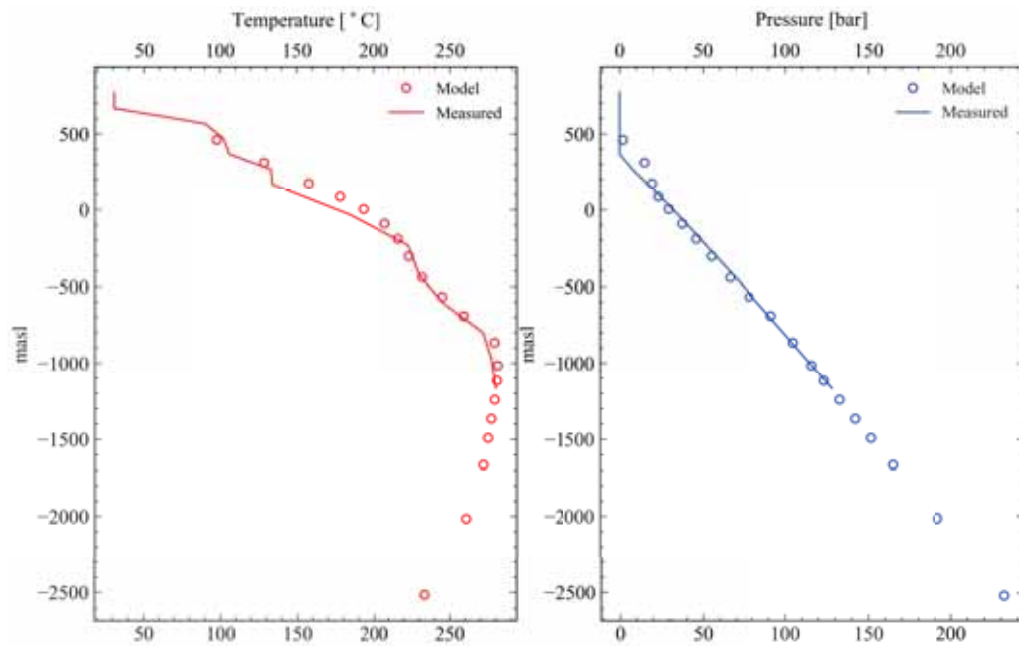
Figure 5.3: Formation conditions for well TR-4C, grey lines represent previous stages during the calibration process.
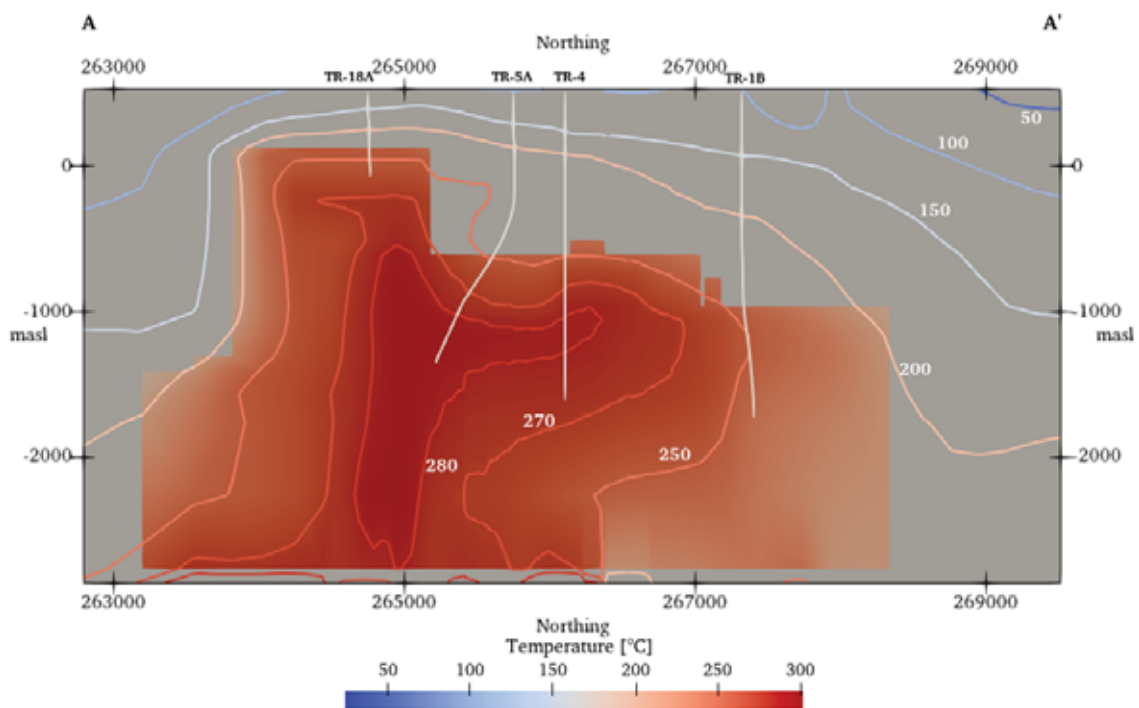
Figure 5.4: Vertical cross section of natural state temperature distribution, over line A-A' in Figure 4.6, white lines represent wells tracks and labels over contour plots temperature in Celsius.

5.2. Production state

The outcome from the natural state serves as an input to the mass extraction stage, where several disturbances in the system are included in the form of sources and sinks. In this stage, one of the main outputs is permeability distribution and values; the latter was accomplished by having some permeability values as a list of parameters and estimates through an inversion in iTOUGH2, using time-series from the production state and P&T formation values. Previous inversions, including only formation values in general, showed lower permeability values.

The permeability values are presented in Table 5.1; some permeabilities, such as the ones assigned to the basement, surface, and outer field, were kept constant. The permeability distribution from selected layers is presented in Appendix A.3.

Table 5.1: Permeability values.

Rocktype	Horizontal permeability [mD]	Vertical permeability [mD]
RESU1	7.43×10^{-3}	7.43×10^{-3}
RESU2	1.25	2.98
U2STH	370.48	223.75
RESU3	3.12×10^{-2}	3.12×10^{-2}
RESU4	37.03	33.41
NSFLT	79.13	72.45
EWFLT	63.28	43.69
BARRI	1.50×10^{-2}	1.50×10^{-2}
U2FRC	8.15	5.30
U4NRT	6.09	28.52
U4EST	11.16	38.50
U4UPF	38.20	36.40
U3STH	4.89×10^{-2}	4.78×10^{-2}
RESBR	0.184	0.291
U2CNV	8.89	9.97

The 2016 event described in Section 3.7 was reproduced by reassigning the elements associated with both rock types RRSU4 and U4UPF to another material REU46, with permeability values of 18 mD and 32 mD in horizontal and vertical direction. The described process allows to increase boiling in the South (Figure 5.17) and increases the pressure drawdown in the Center of the field(Figure 5.5). The higher permeabilities within the geothermal reservoir are found at the steam cap, represented by U2STH, and the lower values at the barriers (BARRI). The rocks related to the production and upflow zone present values ranging from 18 to 79 mD. Moreover, the permeability at the injection area ranges from 6 to 28 mD. Figure 5.3

presents the comparison in time between the calculated pressure drawdown and the monitoring pressure over time; the model response is somewhat fast to the changes in mass extraction. However, the model agrees with the trends and values from the monitoring pressure quite well.
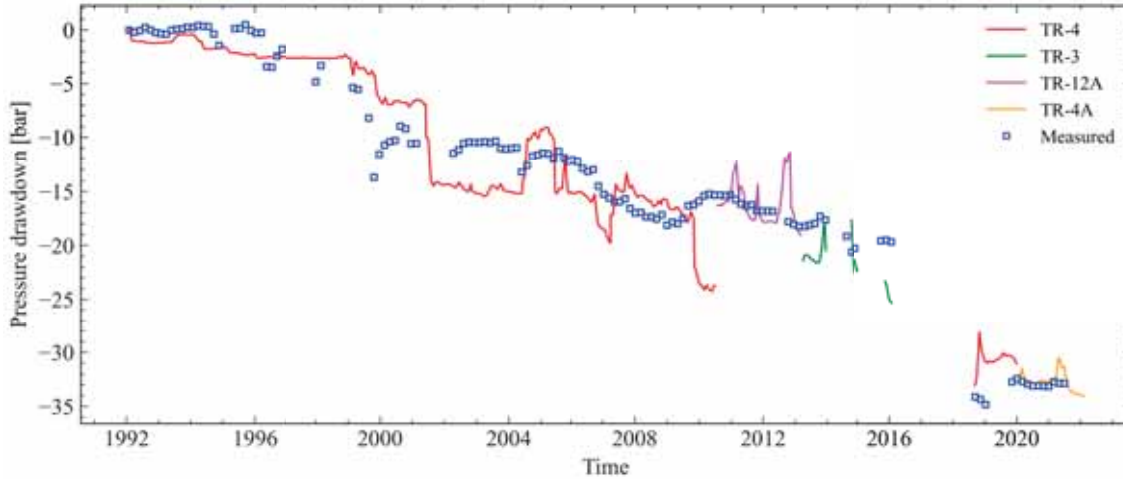
Figure 5.5: Pressure drawdown history matching as one time-serie for different monitoring wells.

Figure 5.6 compares the measured and calculated enthalpy from the production wells; a frequency distribution on each axis shows the enthalpy distribution for the two groups of producer wells: center and south. The center in the model produces from liquid and the south from a somewhat lower temperature. However, the south presents biphase and steam saturation conditions at 1700 and 2750 kJ/kg. The flowing enthalpy history matching for the production wells can be found in Appendix A.2.

During the calibration process, steam wells kept their saturation condition for only a few years after production started due to the reduction in pressure and the consequent fluid migration from below. Three different approaches were tested: increased porosity, permeability, and enlarged steam cap extension. The first and second did not prevent the steam saturation reduction, while the latter allowed the wells to yield enough steam. The different behaviors are presented in Figure 5.7, this indicates that the steam cap volume might extend to the south and between well pads TR-17 and TR-18.

Before the wellbore simulator was incorporated into the model, a sensitivity analysis was performed where the parameters RESU4_XY, U4NRT_XY and RESU3_XYZ resulted as largest contributors to the objective functions. It is important to mention that RESU3_XYZ represents the caprock for the steam wells, which from Table 5.1 turns out to be slightly higher than caprock permeabilities for the rest of the field, most likely to allow a subtle interaction between the shallow aquifer and the steam wells.
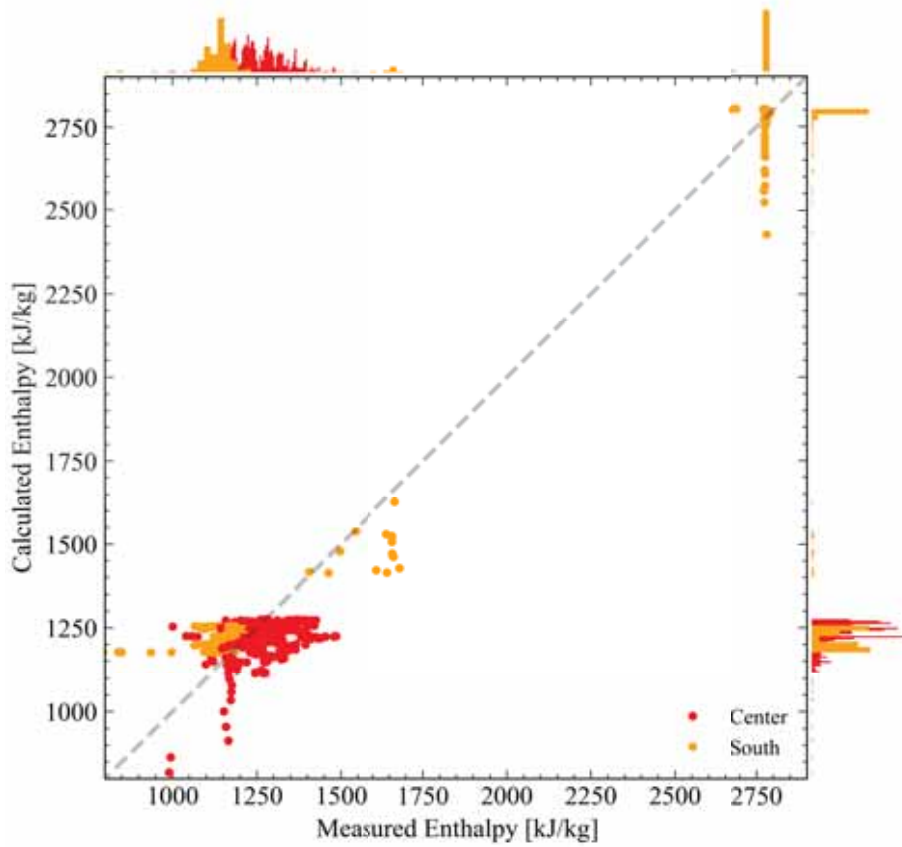
Figure 5.6: Scatter enthalpy plot for producing wells from South and Center areas.
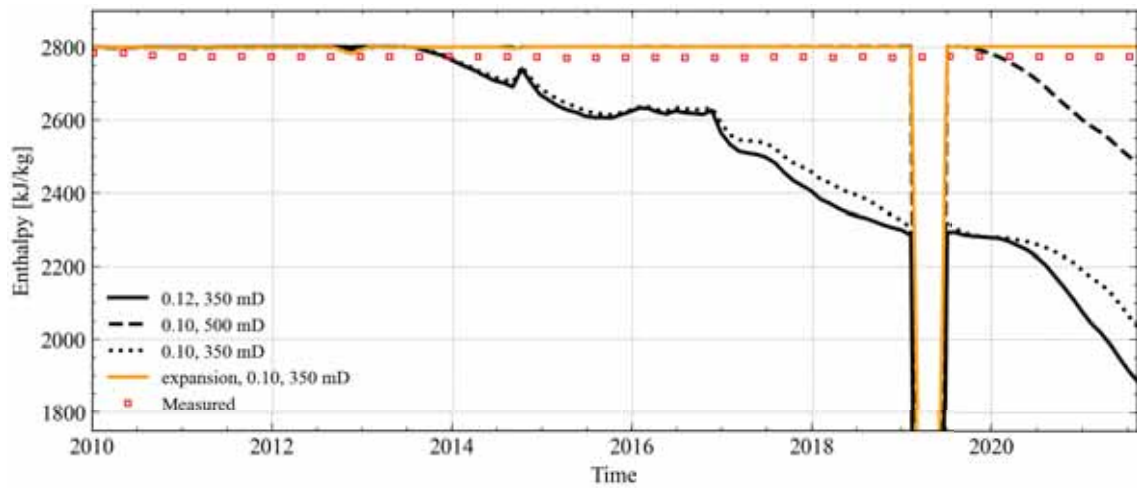
Figure 5.7: Flowing enthalpy evolution during calibration for well TR-18A.

Moreover, the observation datasets that contributed the most to the objective functions were: TR-4 enthalpy, TR-9 drawdown, and monitoring pressure. Figure 5.8

shows the objective function behavior against the evaluation of four parameters in a log-log plot; the red lines represent the path of the parameters through five iterations. Figure 5.8a defines the objective function contours for the least sensitive parameters: `BARRI_XYZ` and `EWFLT_XY`, it shows the path during five iterations which seems to be parabolic around the same coordinates. Whereas, Figure 5.8b presents a pair of the most sensitive parameters the movement, in this case, there is a straight line heading the local objective function minimum.
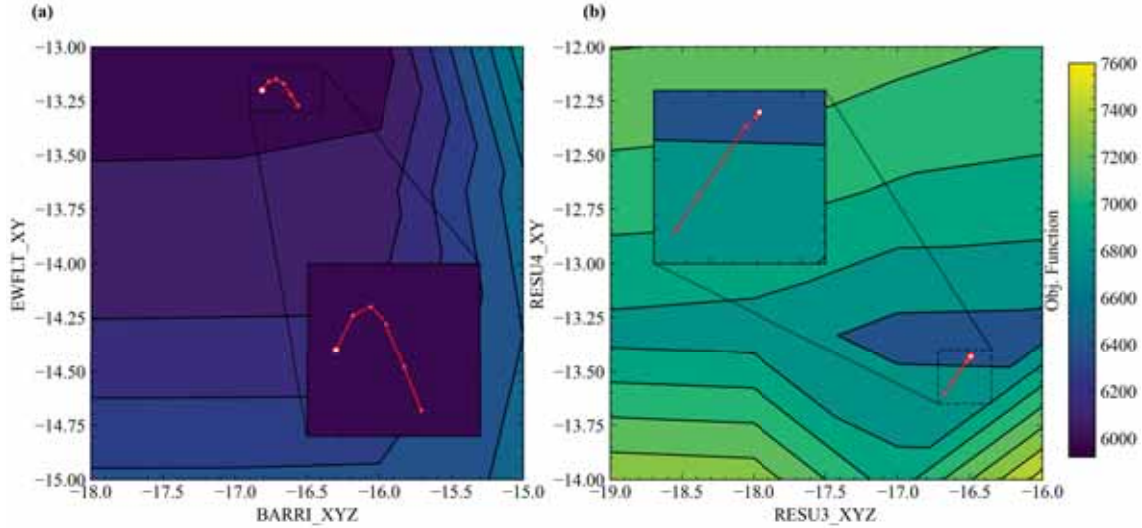
Figure 5.8: Grid search for four parameters (a) low sensitive parameters (b) most sensitive parameters. Red line represents the path through the inverse modeling iteration of each pair of parameters.

The matrix of direct correlations from the error analysis indicates to which extent the change in another parameter can compensate for the variation of one parameter. Some of them might exhibit preferential correlation due to the available data, e.g., during the calibration process, a barrier was introduced between the production zone and injection zone to avoid the rise in pressure observed during injection and allow to increase the permeability in the injection zone. Thus, the parameters `BARRI_XYZ` and `U4NRT_XY` present a negative correlation. Additionally, the correlation chart strongly relates (0.7) the permeabilities associated with the caprock and shallow aquifer since the decrease in one allows the other to keep the reservoir confined. Nevertheless, for the reservoir rocks, the correlations are lower than 0.6.

5.2.1. Coupled wellbore simulator

For this stage, all the wells were defined as described in Section 4.3. The simulator is used in active mode; hence, for the multifeedzone wells, flow redistribution is expected. Due to the complexity of the model, inversions accounting for a minimum of

parameters, e.g. productivity indexes and permeabilities, were very computationally demanding. Therefore, the productivity indexes were adjusted manually, and the permeabilities found during the production state were kept constant. Furthermore, high productivity indexes were required for some liquid wells due to the reduction in enthalpy over time. Thus, some wells were set only as MASS source type.

The minimum pressure was established depending on the historical WHP data. For most of the wells feeding Unit 1 and 2, WHP was set to 11 bar whereas for Unit 3, around 9 bar. Figure 5.9 shows a scatter plot between all the calculated and measured WHP. It can be seen most of the measured values ranges from 8 to 11 bar, unlike the calculated where the values are concentrated around 15 to 16 bar. These results are attributed to the selection of constant productivity indexes for long production periods and the assumption that the well head valve is wide at all times. Therefore, due to the pressure drawdown, high WHP is calculated in the early stages of production.
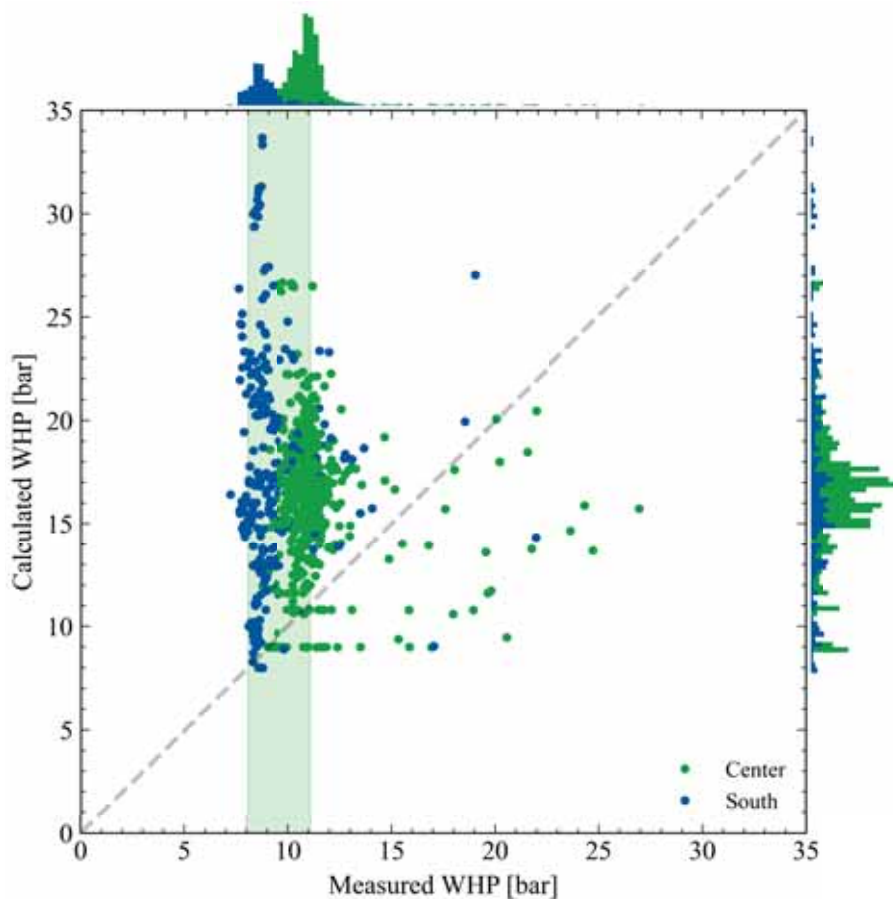
Figure 5.9: Measured and calculated wellhead pressure in producing wells.

Figure 5.10 presents two examples of WHP and flowing enthalpies compared to the wellbore simulator output, (a) shows the flowing enthalpy for well TR-17A,

the difference in enthalpy between the feedzone and wellhead is explained by the pressure drop when the fluid travels in the wellbore due to the effects of friction and gravity. The difference in enthalpy between the model and measurements is due to the lower temperature needed in the area. Since the well PI was defined in two periods: 2007 to 2015 and 2015 to 2021, the WHP (c) matches only during the second period. Although in (b), the enthalpy reaches the observed steam saturation conditions, the model does not reproduce the observed stable WHP around 10 bar.
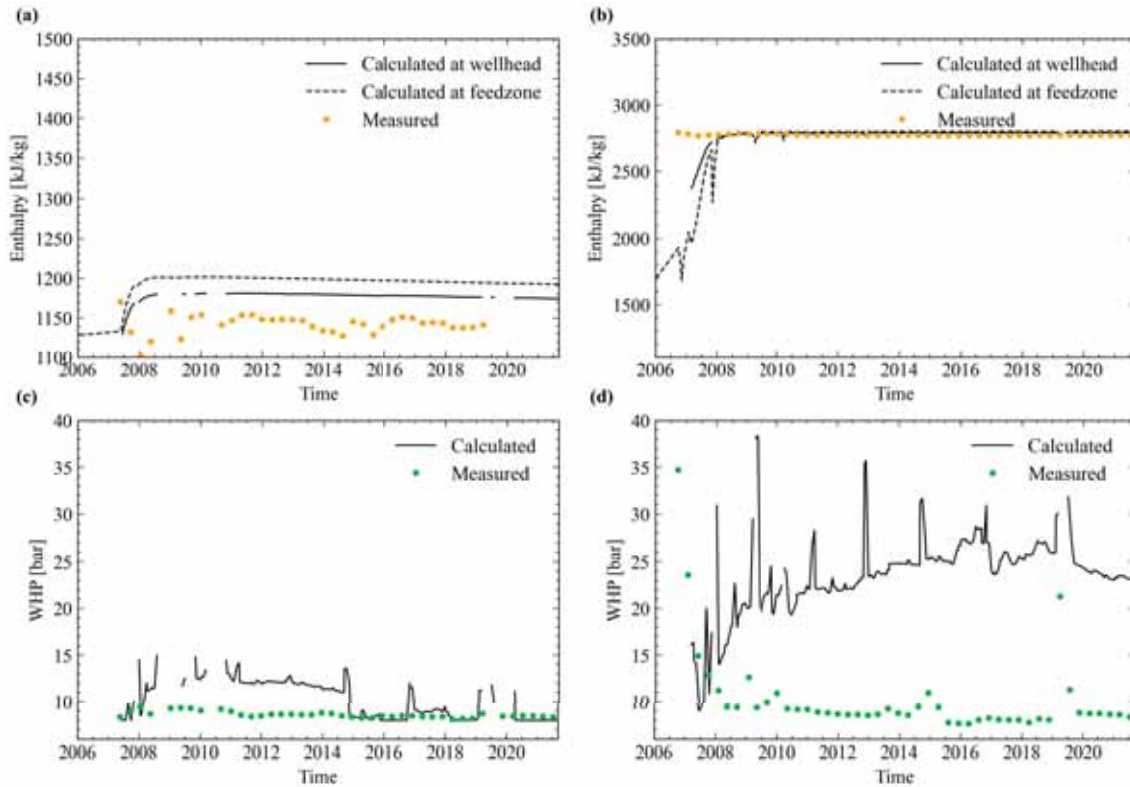
Figure 5.10: Calculated and measured flowing enthalpy for wells TR-17A (a) and TR-18A (b). Calculated and measured WHP for wells TR-17A (c) and TR-18A (d).

Figure 5.11 presents dynamic logs for three different wells. Overall, the pressure and temperature evolution through the wellbore match fairly well in (a) and (c). However, Figure 5.11 (b) presents a higher calculated pressure and temperature as a result of the low presence of boiling in the area.
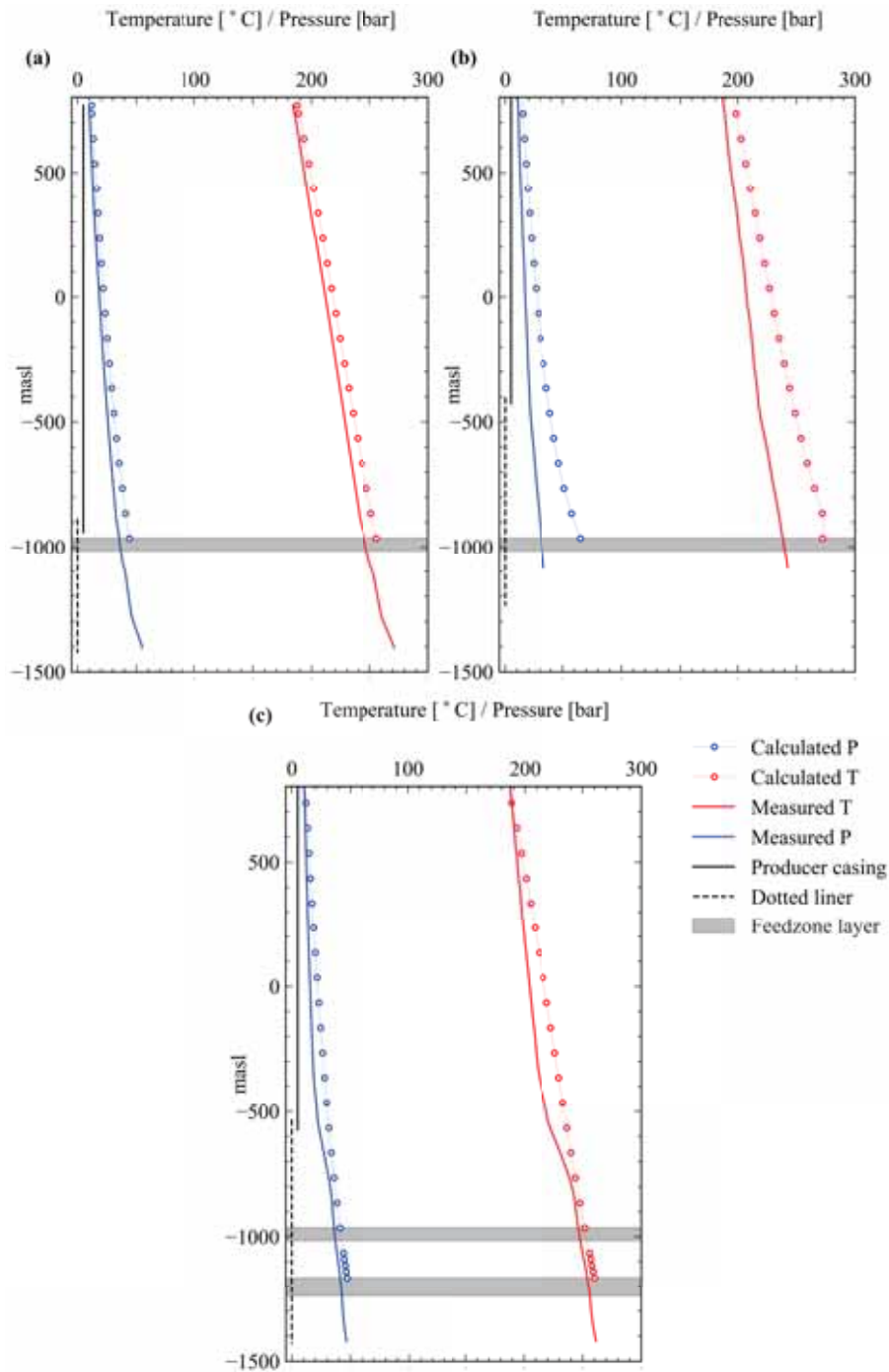
Figure 5.11: Calculated and measured dynamic logs comparison for (a) TR-4B on 2019-12-05, (b) TR-5 on 2011-07-06, and (c) TR-5 on 2020-08-19.

5.3. Forecasting

Results from production scenarios presented in Section 4.8 are discussed in the following paragraphs. The pressure response located at the main feedzone of well

TR-4A is presented in Figure 5.12. For scenario 1, 92% of the pressure is recovered within eight years after cease of production, while in scenario 2, pressure rises due to the reduction in mass extraction and shutting down of some producer wells. For scenarios 3 and 4, the generation oscillates within a range around the install capacity. Hence, similar pressure drawdown trend is decline in both scenarios. By the end of the simulation time, the pressure seems to continue in a less steep but constant rate. On the other hand, the temperature variation shown in Figure 5.13, estimates a reduction of $6\,^{\circ}\mathrm{C}$ by 2020 and up to $14\,^{\circ}\mathrm{C}$ by 2052 in scenarios 3 and 4. However, when production halts in 2024, the temperature stabilizes and decreases slightly, finally around $90\,\mathrm{y}$, the temperature starts to increase, taking about $600\,\mathrm{y}$ to recover its initial value.
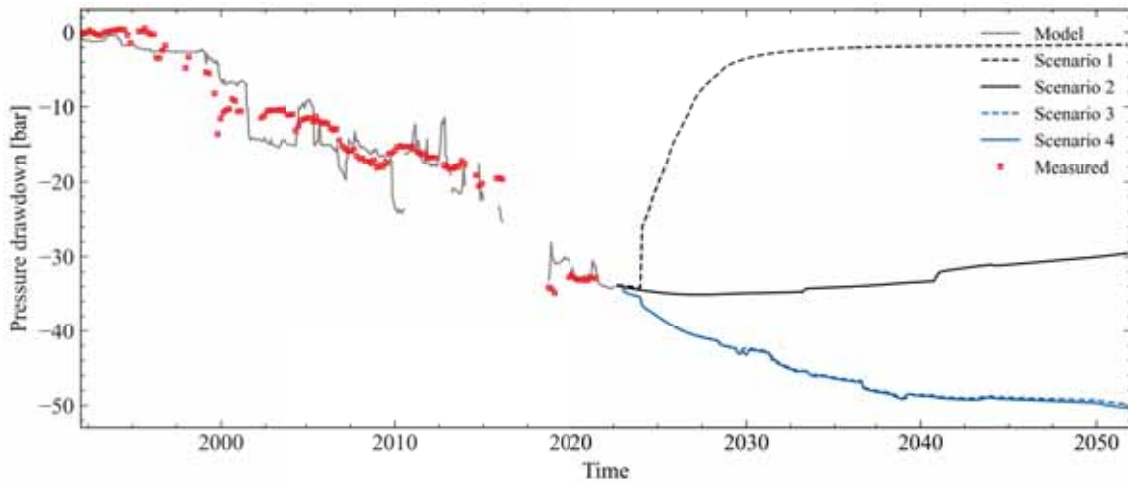
Figure 5.12: Pressure drawdown for different scenarios, after 2022 the pressure is shown in well TR-4A.
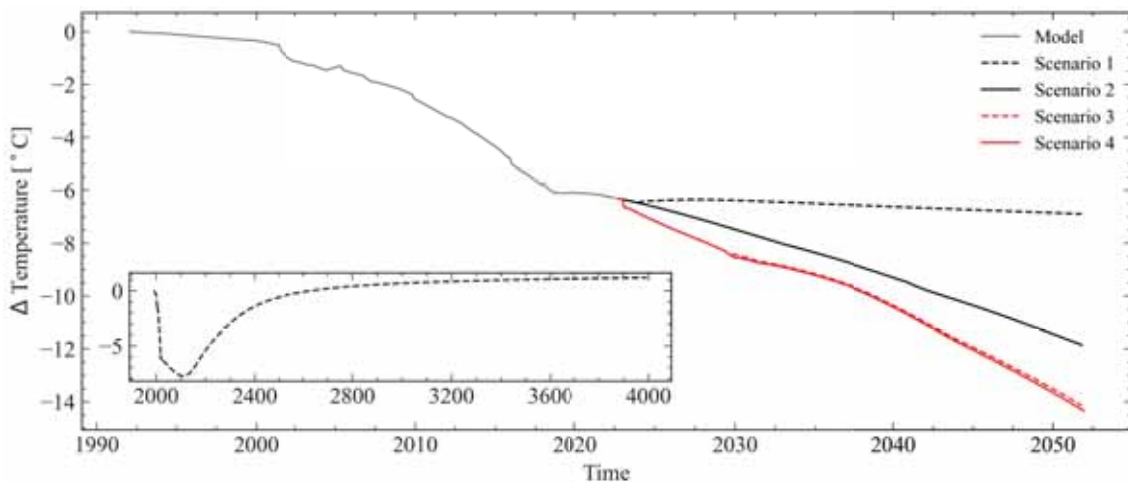
Figure 5.13: Temperature variation for different scenarios at the center of the field, subplot represents the long term temperature recovery for scenario 1.

Figure 5.14 presents the weighted flowing enthalpy based on the mass flow rate for the production wells. For scenario 2, enthalpy decreases after 2036 when most steam wells reduce their production due to pressure decline. Moreover, for scenarios 3 and 4, enthalpy is driven by the introduction of make-up wells from the steam cap.
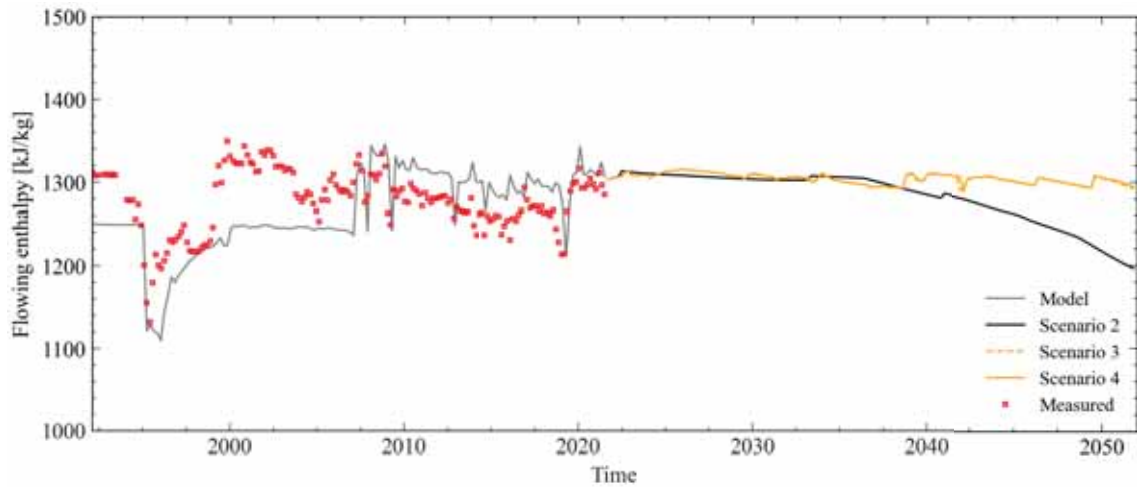
Figure 5.14: Flowing enthalpy history for production wells in different scenarios.

Figure 5.15 contains the wells and mass flow extraction over time added to the model in scenarios 3 and 4. However, as for 2021 well TR-4 is closed and TR-5 produce at a lower capacity than its production history reveals, both wells demand is increased the their previous highest capacity in january 2024. Make-up wells feeding power generation Unit 1 and 2 produce from layers N and M, while the wells for Unit 3 produce from layer F. In all cases, a 9 inch perforated liner and $13\frac{5}{8}$ inch production casing was defined in the wellbore simulator input section. Attempts locate producer wells on the northern side of La Planta Fault, in the proximity of well TR-10 were ineffective due to the low temperature in the area.

Figures 5.16 and 5.17 show power production for wells in the Center (Unit 1&2) and South (Unit 3) respectively. For wells defined in the wellbore simulator, the steam flow rate is directly taken from the wellhead conditions, whereas for the wells defined only as MASS type, an isoenthalpic process is assumed from the reservoir conditions at the well feedzone up to a wellhead pressure of 9 bar for wells connected to Unit 3 and 11 for Units 1 and 2. A specific steam consumption of 1.95 MW/kg/s is used for wells connected to Units 1 and 2 and 2.45 MW/kg/s for Unit 3. For all the units in the second scenario, the power generation declines following the mass extraction reduction. The step-wise reduction shown for Units 1 and 2 is attributed to the cease of production from wells TR-4B and TR-5D. However, the sawtooth shape corresponds to the mass extraction reduction, usually in an existing well, once a new make-up well starts producing. For Unit 3, the reduction after 2036 is attributed to the steam cap collapse due to pressure decline and mass inflow to the southern area.
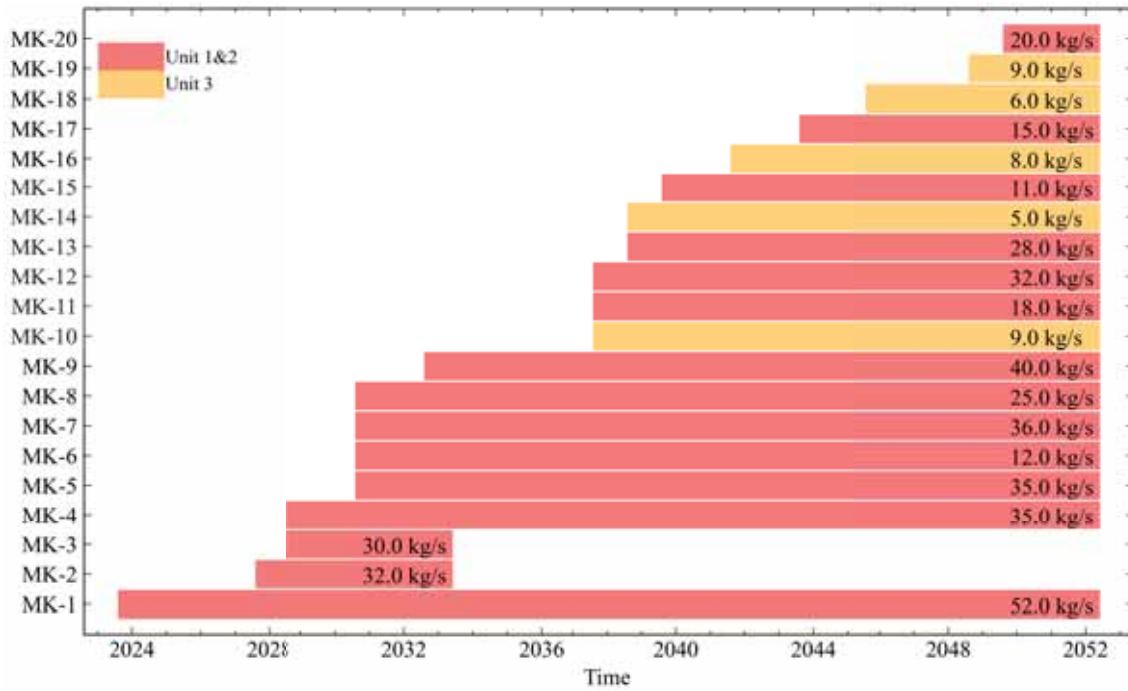
Figure 5.15: Make up wells, red bars are wells connected to Unit 1 and 2.
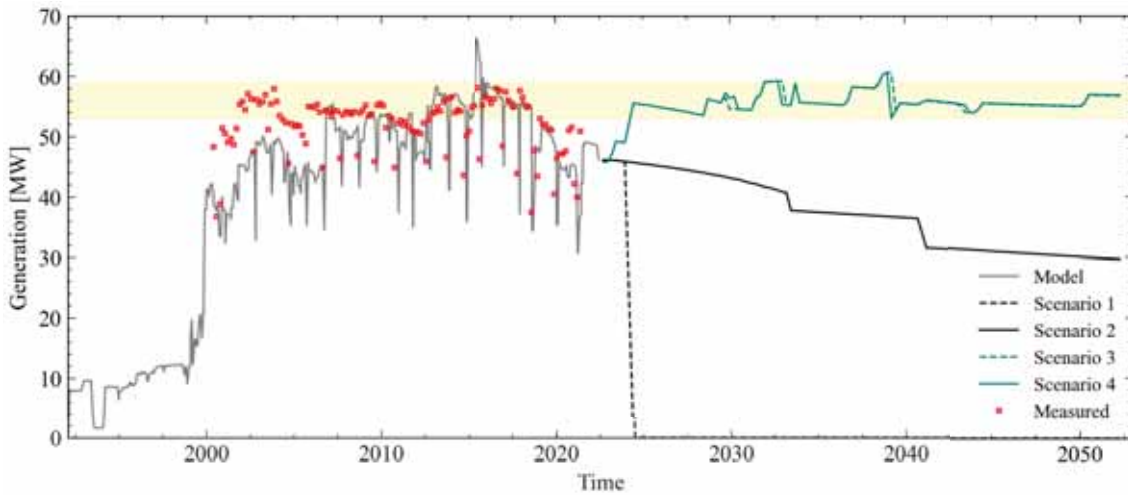
Figure 5.16: Power generation for wells connected to Units 1 and 2 for different scenarios 56 ± 3 MW.

Figure 5.18 (a) shows the initial temperature distribution around the reinjection area. The mass flow rate history from TR-4A shows it has been injecting fluid, at 741 kJ/kg, since March 1999. Therefore, the temperature distribution around the well feedzone shown in Figure 5.18 (c) to (e) stays close to 160 °C. Nevertheless, for the rest of the wells, the flowing enthalpy drops to 330 kJ/kg for the well at the pad TR-19 and 430 kJ/kg for wells TR-1A, TR-1C, and TR-10A in 2024. Hence,
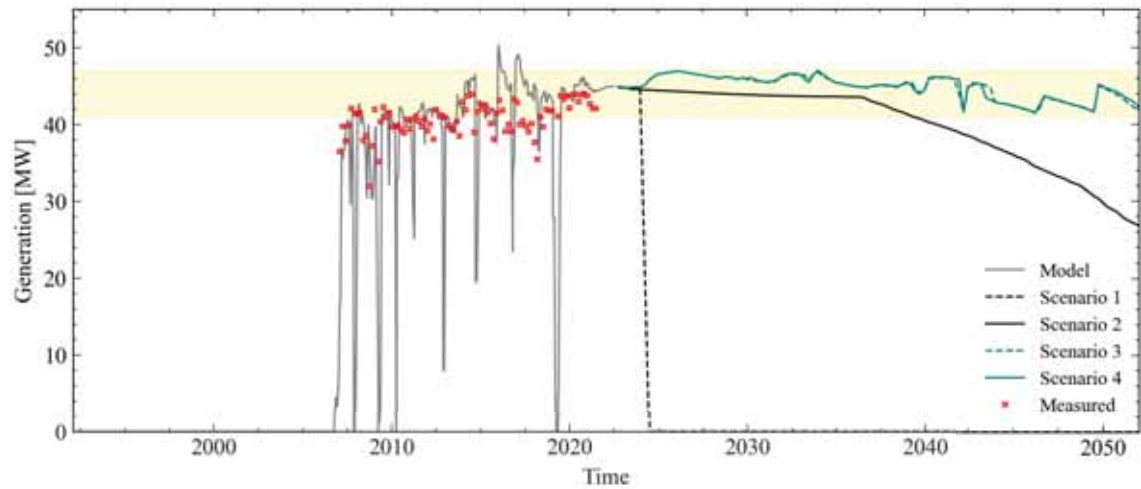
Figure 5.17: Power generation for wells connected to Unit 3 for different scenarios, yellow fill marks the range $44 \pm 3\,\mathrm{MW}$.

the cold front moves southwest, following the convection cell, to the center of the field. However, by 2050 there is no significant difference in the enthalpy or pressure drawdown evolution shown in Figures 5.14 and 5.12 most likely due to the barrier introduced between the production and injection areas and the absence of nearby producing wells in the area.

Figure 5.19 (a) presents vertical cross-section, over D-D' from Figure 4.6, for the initial steam saturation state at the southern side of the field. Figure 5.19 (b) and (c) display the steam saturation evolution during the calibration time, where the steam cap extension and value increase over time. The steam cap collapse for the second scenario is observed from Figure 5.19 (d) to (f) as the volume occupied is reduced. As the extraction is maintained due to the drilling of new makeup wells in scenarios three and four, the steam cap volume keeps increasing, reaching completed saturation conditions by 2052 in five layers below the caprock at the TR-18 well pad, at the same time, there is no visible impact of the cold front generated in scenario four at the steam wells.
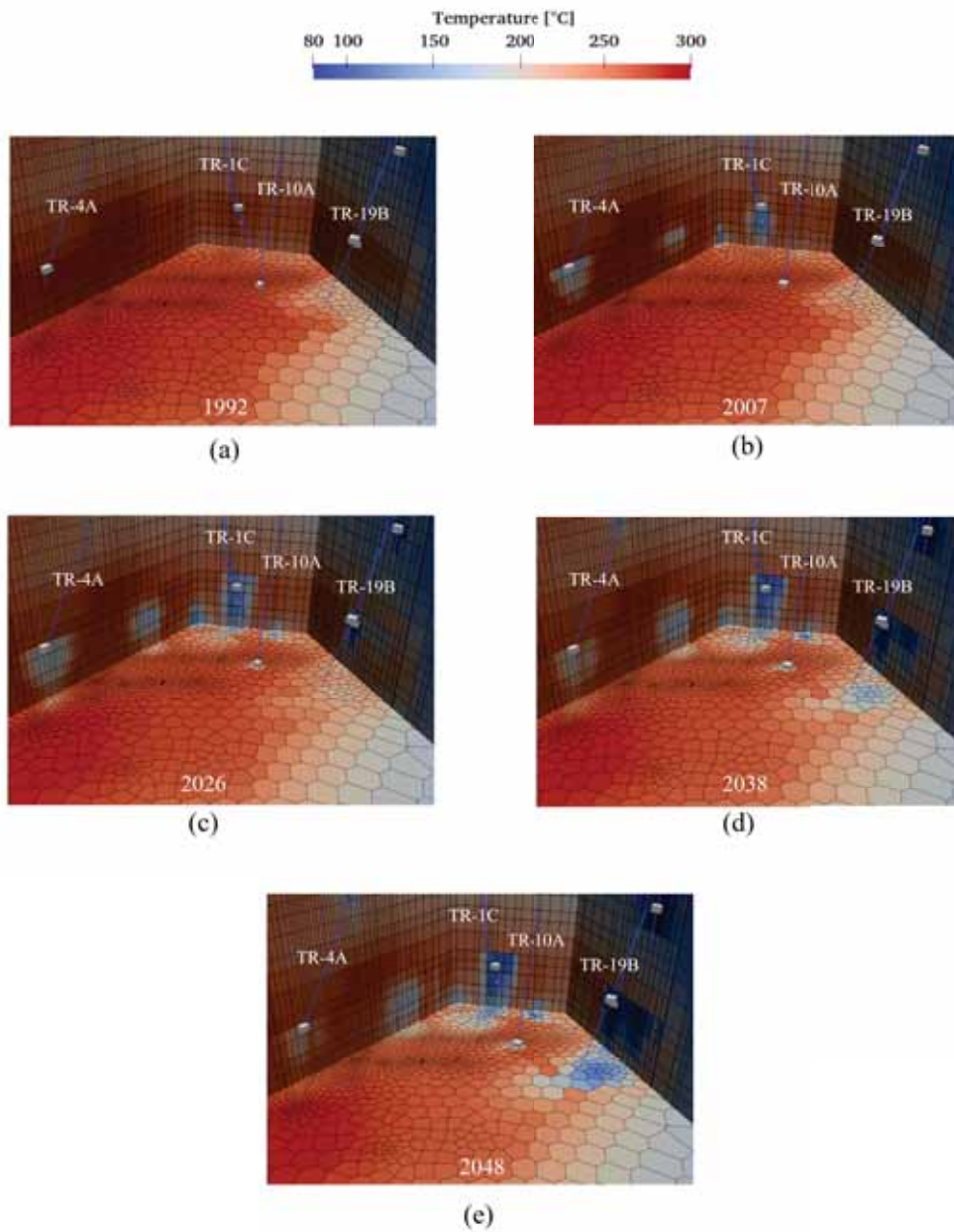
Figure 5.18: *Temperature evolution around reinjector wells for the years (a) 1992 and (b) 2007. Temperature distribution in (c) 2026 (d) 2038 and (e) 2048 for scenario number four.*
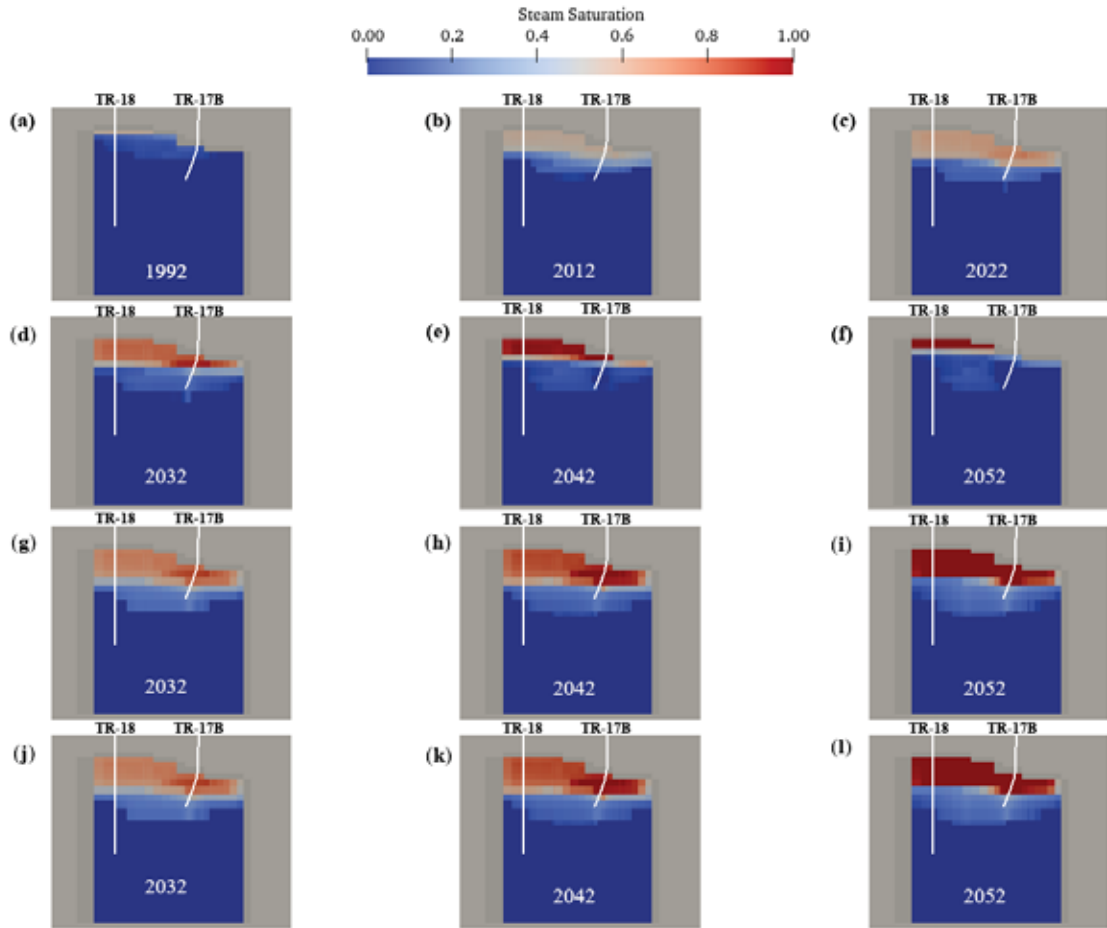
Figure 5.19: Steam saturation evolution, over line D-D' from Figure 4.6, (a) to (c) represent the base model, (d) to (f) scenario 2, (g) to (i) scenario 3 and (j) to (l) scenario 4. Grey color represents elements outside the main geothermal reservoir and white lines wells tracks.

6. Discussion

A prior study attributed the steep pressure decline observed at the monitoring well TR-4 compared with the minor drawdown in the first years of production to a boiling process [39]. The current study was able to reproduce such behavior by developing a steam cap in the southern side of the field between the well pads TR-17 and TR-18 and the northern flanks of the Tecapa volcanic complex.

The heterogeneity of the geological structures is represented by the permeability distribution and optimized by the parameterization and subsequent modeling inversion using iTOUGH2 and formation and production time series. The permeability presents anisotropy, and the values ranges for the geothermal reservoir range from 6 to 79 mD, between 370 to 223 mD for the steam cap and 3.12×10^{-2} mD, for the caprock which is in range of other geothermal reservoir models in similar geological setting [62, 7, 29]. This study also evaluates the production wells using the built-in wellbore simulator FLOWELL in TOUGH2. This allows calibrating of the productive indexes of most of the producer wells and the flow distribution in the identified feedzones. Furthermore, four production scenarios are evaluated, focusing on maintaining the power production at the same level for the next 30 years, founding a pressure decline at the center of the field of 10 bars, and the need to drill 20 make up wells over time. Layer F (40 to 140 mbsl) and N (1065 to 1165 mbsl) were used as primary feedzone locations mainly between the TR-5's and TR-17's for the makeup wells, which slowly enlarged the steam cap volume.

The main features presented by the conceptual model were reproduced, including the geothermal reservoir delineation by the magnetotelluric resistivity anomaly, stratigraphy, recharge and outflow location. Nonetheless , the hot inflow was located up north from the estimated location due to the vertical extension, with the aim of reproducing the hot plume observed in the well pads TR-5 and TR-4.

Scenario one indicates that a cease in production would allow the field to recover about 92% of its initial pressure in nearly eight years in the center of the field. As expected, temperature is recovered in a different time scale (600 y). In the other hand, without keeping up with the mass flow extraction, represented by scenario two, steam cap eventually collapses due to the fluid inflow at the higher layers on the southern side of the field caused by the pressure drawdown and overall enthalpy reduction.

7. Conclusions

This project developed a detailed numerical coupled wellbore-reservoir model for the Berlin Geothermal Field in El Salvador. The reservoir simulator TOUGH2 and the built-in wellbore FLOWELL simulator were used. The model was calibrated making use of formation conditions of 39 wells, 32 time-series from producer wells including flowing enthalpy, and well head pressure, and 4 time-series from monitoring wells from 1992 to 2021. Overall, a good agreement between the model and the historical data is achieved for the wells on the production side of the field. Nevertheless, for wells at the northern borders of the drilled area further improvement in calibration can be performed. The parameter estimation using iTOUGH2 enhanced the calibration especially for the observation points related with the production state. The sensitivity analysis results shown the highest contributor to the objective function as the rock permeabilities associated with the main geothermal reservoir and the cap rock.

The stratigraphy distribution and formation conditions indicates the conditions to generate a permeability distribution such that the steam cap in the southern side of the field could be reproduced. It started with a slight steam saturation prior exploitation and enlarged its volume due to mass extraction in the Center and South areas of the field. For long term production, four scenarios were formulated using calibrated numerical model. The first scenario estimates 92% pressure recovery within eight years after shutting down the production and injection in the field. The second forecasting considers maintaining the same number of producing wells as 2021, a step-wise decrease in power generation is observed, where the steepest decline corresponds to the shut down of some producer wells due to pressure drawdown. The third and fourth scenario considers maintaining the production and injecting colder brine coming from the well pads TR-17 and TR-18 for the latter. In both cases, it was possible to maintain the production within ± 3 Megawatt (MW) margin for every generation unit. By maintaining the energy production, some of the current wells eventually cease their mass extraction due to pressure drawdown. In both scenarios, due to the constant mass extraction, the steam cap enlarged. However, some new wells are eventually needed to maintain the power production of Unit 3.

For all the simulation time, including calibration and forecasting, wells were treated using the wellbore simulator. It was found that while using the wellbore simulator, the model runtime significantly increased up to a factor of three for a converging

model. Nevertheless, the direct coupling provides better insight for both single and multifeedzone wells mass flow rate extraction due to pressure drawdown and cooling. Therefore, the approach used in this study is recommended to become part of the standard procedure for numerical models of the geothermal reservoir calibration process in the future when enough data for calibration is available.

Further improvements in the model involve including the chemical process occurring in the vicinity of the wellbore, which would locally decrease the formation pressure and well productivity, as well as the use of a different Equation Of State (EOS) to simulate the presence of non-condensable gases content. The wellbore simulator's detailed estimation of feedzone location, mass flow rate contribution, and complete history of wellhead valve operation and workovers could improve the wellhead data match and reduce the model runtime. Furthermore, the possible parameter compensation [31] due to the establishment of a heat source at shallow levels should be studied by enlarging the vertical model extension.

References

[1] M. Antics and P. Ungemach. "Quantifying Risk in Geothermal Development – High Enthalpy and Low Enthalpy Cases". In: *Proceedings World Geothermal Congress 2010*. Indonesia, 2010.

[2] A. Arias et al. "Conceptual Model Review of the Berlin Geothermal System (El Salvador)". In: *Geothermal Resources Council Transaction* (Oct. 2003), pp. 755–760.

[3] S. Arnórsson, S. Thórhallsson, and A. Stefánsson. "Utilization of Geothermal Resources". In: *The Encyclopedia of Volcanoes*. Second Edition. Elsevier, 2015, pp. 1235–1252.

[4] L. Barrios, E. Henríquez, and A. Quezada. "Stratigraphic, tectonic and thermal mapping through geological well logging in El Salvador". In: *Short Course on Conceptual Modelling of Geothermal Systems*. Santa Tecla, El Salvador, Mar. 2013.

[5] D. R. H. Beattie. "A note on the calculation of two-phase pressure losses". In: *Nuclear Engineering and Design* 25 (1973), pp. 395–402.

[6] Grimur Bjornsson et al. "Development of 3-D geothermal reservoir model for the greater Hengill Volcano in SW-Iceland". In: *Proceedings, TOUGH Symposium 2003*. California, USA, May 2003.

[7] D. Bowyer and R. Holt. "Case Study: Development of a Numerical Model by a Multi-Disciplinary Approach, Rotokawa Geothermal Field, New Zealand". In: *Proceedings World Geothermal Congress 2010*. Bali, Indonesia, 2010.

[8] J. Burnell et al. "Future directions in geothermal modelling". In: *New Zealand Geothermal Workshop 2012 Proceedings*. Auckland, New Zealandy, 2012.

[9] T. Campos. "Wellhead Units and Geothermal development in El Salvador". In: *Proceedings World Geothermal Congress 1995*. Florence, Italy, May 1995.

[10] Oscar Cideos. "Predictive techniques applied to geothermal power plants data". MA thesis. Reykjavík, Iceland: University of Iceland, June 2015.

[11] A. Corey. "The Interrelations Between Gas and Oil Relative Permeabilities". In: *Producers Monthly* 19 (1954), pp. 38–41.

[12] A. Croucher et al. "Waiwera: A parallel open-source geothermal flow simulator". In: *Computers and Geosciences* 141 (2020).

References

[13] F. D'Amore and J. Tenorio. "Chemical and physical reservoir parameters at initial conditions in Berlín geothermal field, El Salvador: A first assessment." In: *Geothermics* 28 (1999).

[14] Charles DeMets. "A new estimate for present-day Cocos-Caribbean plate motion: Implications for slip along the Central American volcanic arc". In: *Geophysical Research Letters* 28 (2001).

[15] Ronald DiPippo and Joel L. Renner. "Geothermal Energy". In: *Future Energy (Second Edition)*. Second Edition. Elsevier, 2014, pp. 471–492. DOI: `https://doi.org/10.1016/B978-0-08-099424-6.00022-3`.

[16] Vatnaskil Consulting Engineers. *Steinar 7.7*. Reykjavík, Iceland, 2015.

[17] Stefan Finsterle. *Enhancements to the TOUGH2 Simulator Integrated in iTOUGH2*. Lawrence Berkeley National Laboratory. Berkeley,, California, 2017.

[18] Stefan Finsterle. *iTOUGH2 User's Guide*. Lawrence Berkeley National Laboratory. Berkeley,, California, 2007.

[19] GENZEL. "Development of complementary geo-scientific studies in Berlín geothermal field". 1995.

[20] Malcolm Grant and Paul Bixley. *Geothermal Reservoir Engineering*. 2nd ed. ELSEVIER, 2011. ISBN: 9780128103753.

[21] Maria Gudjonsdottir. ""Assessing relative permeabilities in geothermal reservoirs using theoretical relations, laboratory measurements and field data". PhD thesis. Reykjavík, Iceland: University of Reykjavík, Nov. 2015.

[22] Halldóra Guðmundsdóttir et al. *iTOUGH2-FLOWELL: Simulating Wellhead Conditions Coupled to Geothermal Reservoir User's Guide*. Lawrence Berkeley National Laboratory. Berkeley,, California, 2018.

[23] G. Gunnarsson, A. Arnaldsson, and A. Oddsdóttir. "Model Simulations of the Hengill Area, Southwestern Iceland". In: *Transp Porous Med* 90 (2011).

[24] C Haukwa. *AMESH: a mesh creating program for the integral finite difference method. User's manual*. Lawrence Berkeley National Laboratory. Berkeley,, California, 1998.

[25] José Henríquez. "An update on the Geothermal Development in El Salvador". In: *30th anniversary worshop*. Reykjavík, Iceland, Aug. 2008.

[26] Baltazar Hernández. "Aquifer fluid compositions at the Berlín Geothermal Field, El Salvador in 2012". In: *Geothermal Training Programme* (2012).

[27] Tadao Horie. "Berlin Geothermal Power Plant". In: *Fuji* (2001).

[28] Roland Horne et al. "Steam-water relative permeability". In: *Proceedings World Geothermal Congress 2000*. Kyushu - Tohoku, Japan, June 2000.

56

[29] S. Jalilinasrabady et al. "Development of the optimun numerical reservoir model of the Takigami Geothermal Field, Oita, Japan". In: *Proceedings, Thirty-Sixth Workshop on Geothermal Reservoir Engineering0*. Stanford, California, 2011.

[30] Erick Jiménez. "T2GEORES: A Python Library to Manage TOUGH2 Simulations on Geothermal Systems". In: *World Geotheral Congress 2020+1*. Reykjavík, Iceland, Oct. 2021.

[31] P.J. Johnson et al. "Implications of rootless geothermal models: Missing processes, parameter compensation, and imposter convection". In: *Geothermics* 102 (2022). DOI: https://doi.org/10.1016/j.geothermics.2022.102391.

[32] O. Kolditz et al. "OpenGeoSys: An open-source initiative for numerical simulation of thermo-hydro-mechanical/chemical (THM/C) processes in porous media". In: *Environmental Earth Sciences* 37 (2012).

[33] LAGEO. "Conceptual Model of Berlín Geothermal Field, 2012 (In Spanish)". 2012.

[34] Cornelius Lanczos. "Solution of Systems of Linear Equations by Minimized Iterations". In: *Iournal of Resea rch of the National Bureau of Standards* 49 (1952).

[35] Kenneth Levenberg. "A Method for the Solution of Certain Non-Linear Problems in Least Squares". In: *Quarterly of Applied Mathematics* 2 (1944), pp. 164–168. DOI: 10.1090/qam/10666.

[36] M. Manuel and P. Santos. "Conceptual models for the Berlin Geothermal Field". In: *Short Course V on Conceptual Modelling of Geothermal Systems*. Santa Tecla, El Salvador, Mar. 2013.

[37] Jeff Marshall. "The Geomorphology and Physiographic Provinces of Central America". In: vol. 1. Apr. 2007, pp. 75–122.

[38] Mohammed Masum and M. Akbar. "The Pacific Ring of Fire is Working as a Home Country of Geothermal Resources in the World". In: *PIOP Conf. Ser.: Earth Environ. Sci.* (2019).

[39] Manuel Monterrosa. "A 3-D natural state modelling and reservoir assessment for the Berlin Geothermal Field in El Salvador, C.A." In: *Geothermal Training Programme* (1993).

[40] Manuel Monterrosa. "Reservoir modelling for the Berlin Geothermal Field El Salvador". In: *Twenty-Seventh Workshop on Geothermal Reservoir Engineering*. Stanford University, Stanford, California, Jan. 2002.

[41] M. O'Sullivan, K. Pruess, and M. Lippmann. "State of the art of geothermal reservoir simulation". In: *Geothermics* 30 (2001).

[42] M. Pham et al. "ECLIPSE Geothermal - A Next-Generation Geothermal Reservoir Simulator". In: *European Geothermal Congress*. Netherlands, 2019.

References

[43] J.W. Pritchett. "STAR: A geothermal Reservoir simulation system". In: *Proc. World Geothermal Congress 1995*. Florence, Italy, 1995.

[44] K Pruess. "TOUGH2: A general-purpose numerical simulator for multiphase fluid and heat flow". In: (May 1991). DOI: 10.2172/5212064.

[45] K. Pruess, C. Oldenburg, and G. Moridis. *TOUGH2 User's Guide, Version 2.1*. Lawrence Berkeley National Laboratory. Berkeley,, California, 2012.

[46] Roberto Renderos. "Chemical Characterization of the thermal fluid discharge from well production tests in the Berlín Geothermal Field, El Salvador". In: *Geothermal Training Programme* (2002).

[47] J. Rivas, J. Castellón, and J. Maravilla. "Seven Years of Reservoir Seismic Monitoring at Berlín Geothermal Field, Usulután, El Salvador". In: *Proceedings World Geothermal Congress 2005*. Antalya, Turkey, Apr. 2005.

[48] José Rivas. "Seismic monitoring and its application as an exploration tool in the Berlín Geothermal Field, El Salvador". In: *Geothermal Training Programme* (2000).

[49] Victor Rodríguez. "Analysis of temperature and pressure measurements and production data for Berlín Geothermal Field, El Salvador". In: *Geothermal Training Programme* (2005).

[50] S.Z Rouhani and E Axelsson. "Calculation of void volume fraction in the subcooled and quality boiling regions". In: *International Journal of Heat and Mass Transfer* 13.2 (1970), pp. 383–393.

[51] P. Santos and J. Rivas. "Gravity surverys contributinon to geothermal exploration in El Salvador: The cases of Berlín, Ahuachapán and San Vicente areas". In: *Short Course on Surface Exploration for Geothermal Resources*. Santa Tecla, El Salvador, Oct. 2009.

[52] Pedro Santos. "One and two-dimensional interpretation of DC-resistivity data from the Berlín geothermal field, El Salvador". In: *Geothermal Training Programme* (1995).

[53] Zosimo Sarmiento and Benedikt Steingrímsson. "Review on estimated power potential and realistic development of geothermal resources in leading geothermal countries". In: *Short Course on Geothermal Development in Central America – Resource Assessment and EnvironmentalManagement*. 2007.

[54] M. Shook. "TETRAD Reservoir Simulation". In: *Geothermal Energy and the Utility Market = The Opportunities and Challenges for Expanding Geothermal Energy in a Competitive Supply Market*. California, USA, 1992.

[55] Benedikt Steingrímsson. "Geothermal well logging: temperature and pressure logs". In: *Short Course V on Conceptual Modelling of Geothermal Systems*. 2013.

[56] Prabhata Swamee and Akalank Jain. "Explicit eqations for pipe-flow problems". In: *Hydraulic Division (ASCE)* 102 (May 1976), pp. 657–664.

[57]   Elizabeth Torio H. "Petrography and mineral alteration in Berlin Geothermal Field". In: *Thirty-Second Workshop on Geothermal Reservoir Engineering*. Stanford University, Stanford, California, Jan. 2007.

[58]   M. Trefry and C. Muffels. "FEFLOW: A Finite-Element Ground Water Flow and Transport Modeling Tool". In: *Groundwater* 45 (2020).

[59]   UN. *Resolution 70/1, Transforming our world: the 2030 Agenda for Sustainable Development*. 2015.

[60]   UT. *Anuario estadístico 2021*. Tech. rep. Unidad de transacciones, 2022.

[61]   Pauli Virtanen et al. "SciPy 1.0: Fundamental Algorithms for Scientific Computing in Python". In: *Nature Methods* 17 (2020), pp. 261–272. DOI: 10.1038/s41592-019-0686-2.

[62]   Sadiq Zarrouk et al. "Numerical modelling of production from the Poihipi dry steam zone: Wairakei geothermal system, New Zealand". In: *Geothermics* 36.4 (2007). DOI: https://doi.org/10.1016/j.geothermics.2007.03.006.

A. Appendix

A.1. Natural state
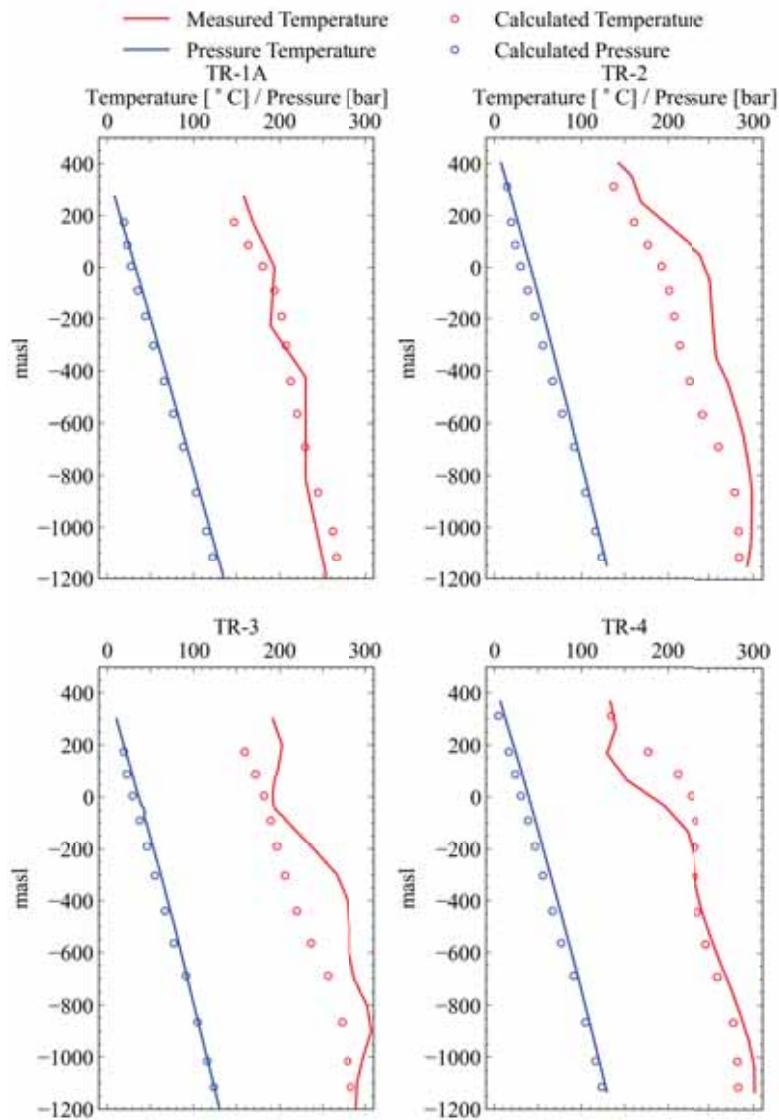
Figure A.1: Natural state plots.
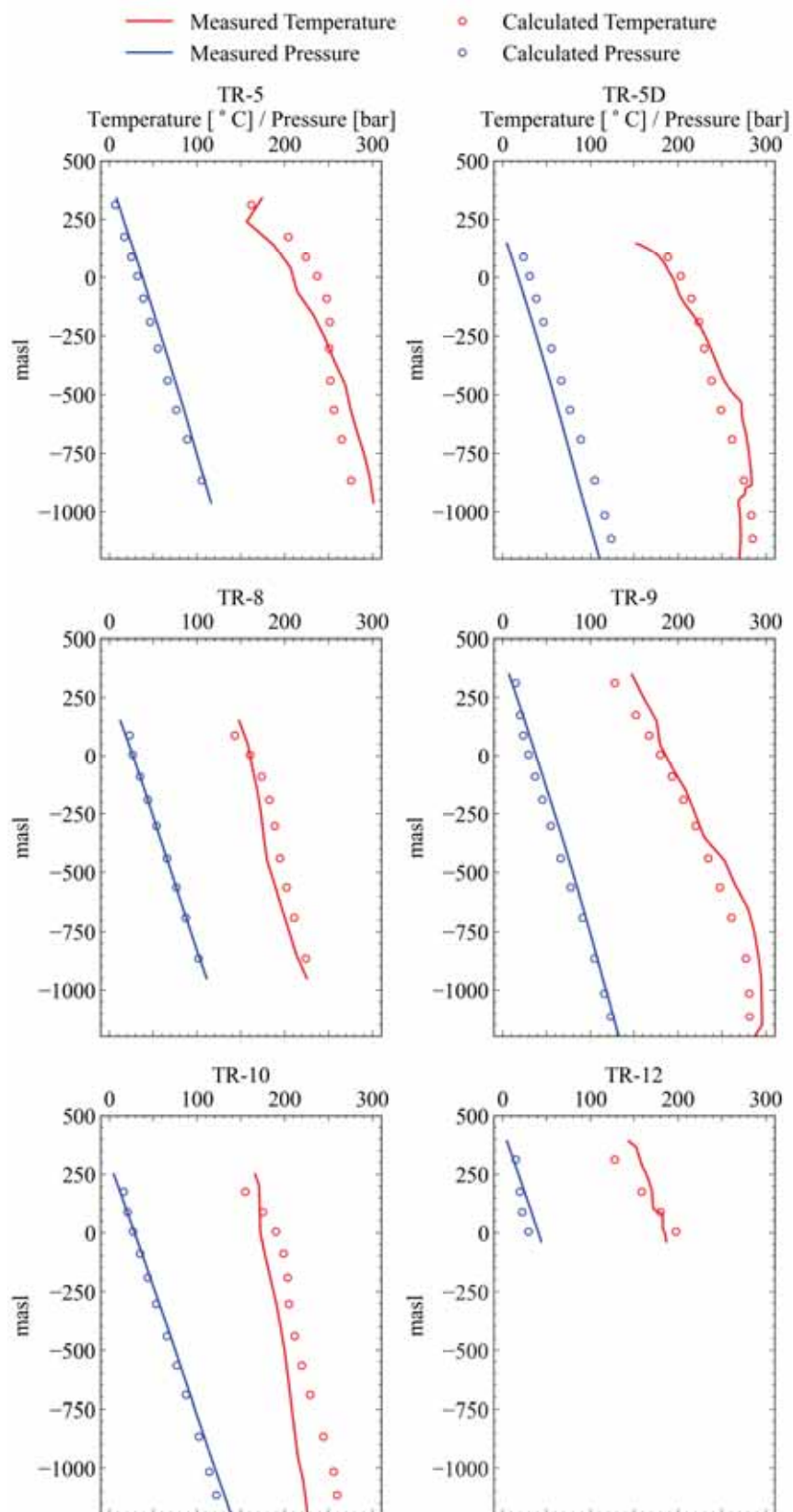
Figure A.2: Natural state plots continuation.
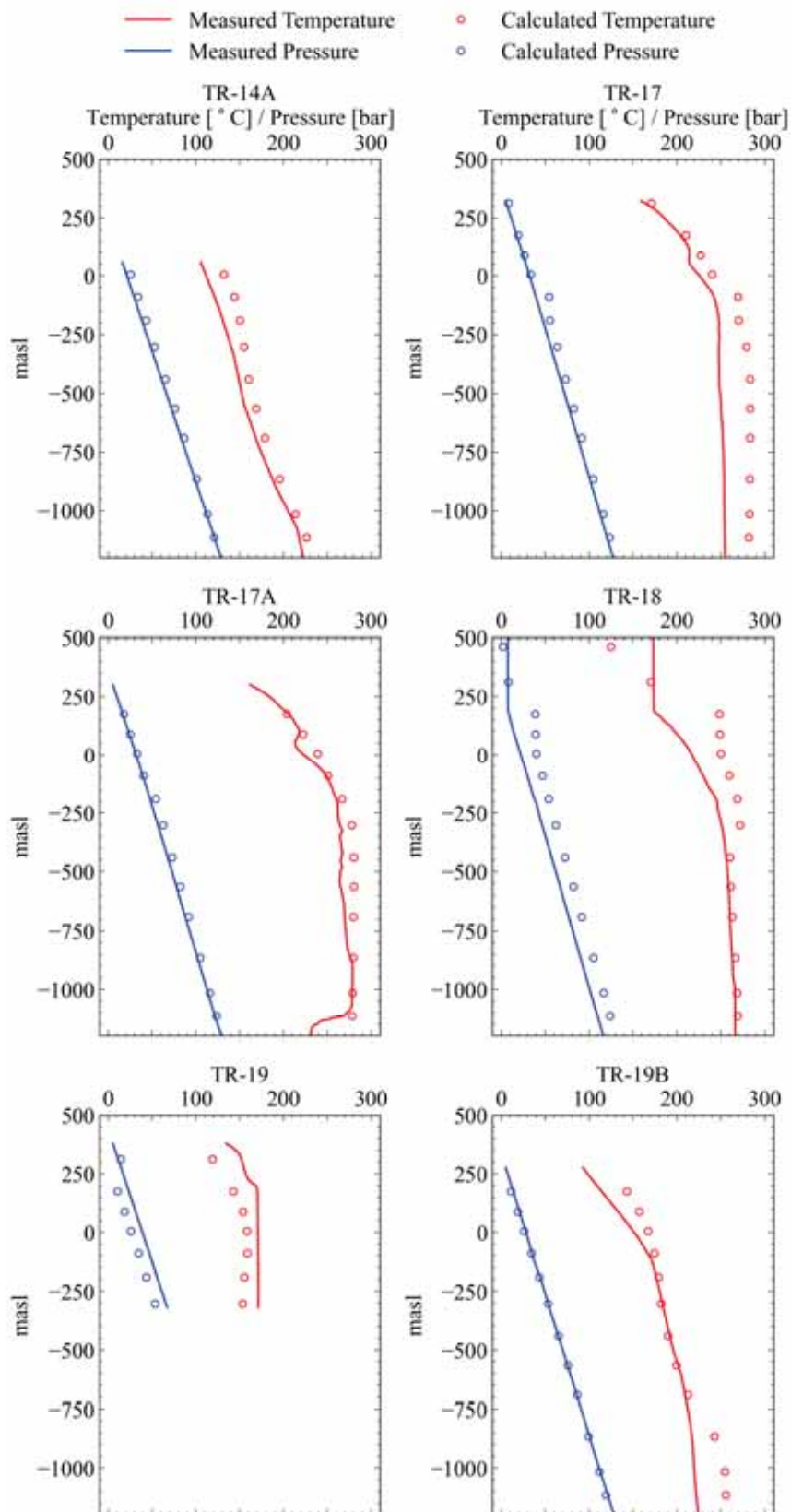
Figure A.3: Natural state plots final

A.2. Production history matching
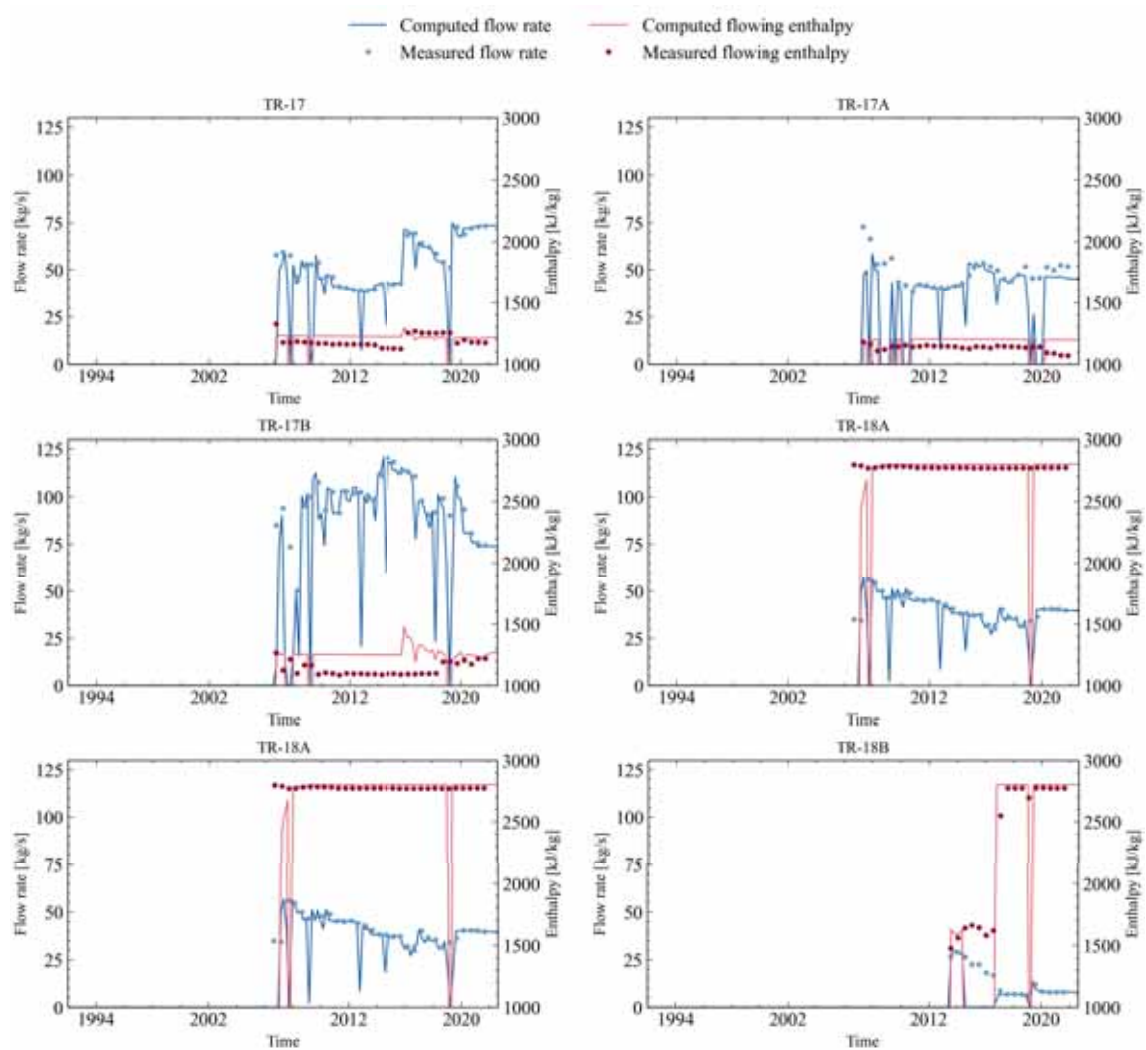
Figure A.4: Mass flow rate and flowing enthalpy for the South area wells.
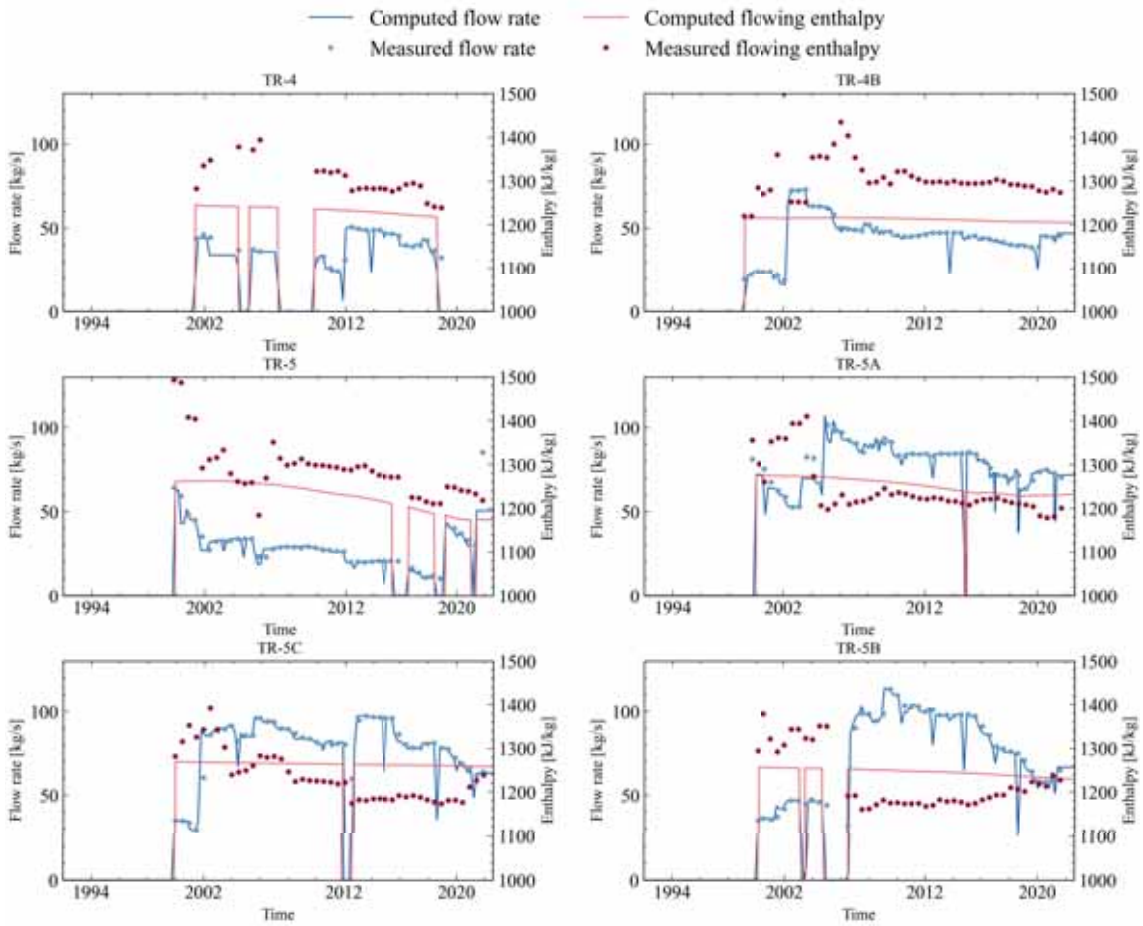
Figure A.5: Mass flow rate and flowing enthalpy for the Center area wells.

A.3. Permeability distribution
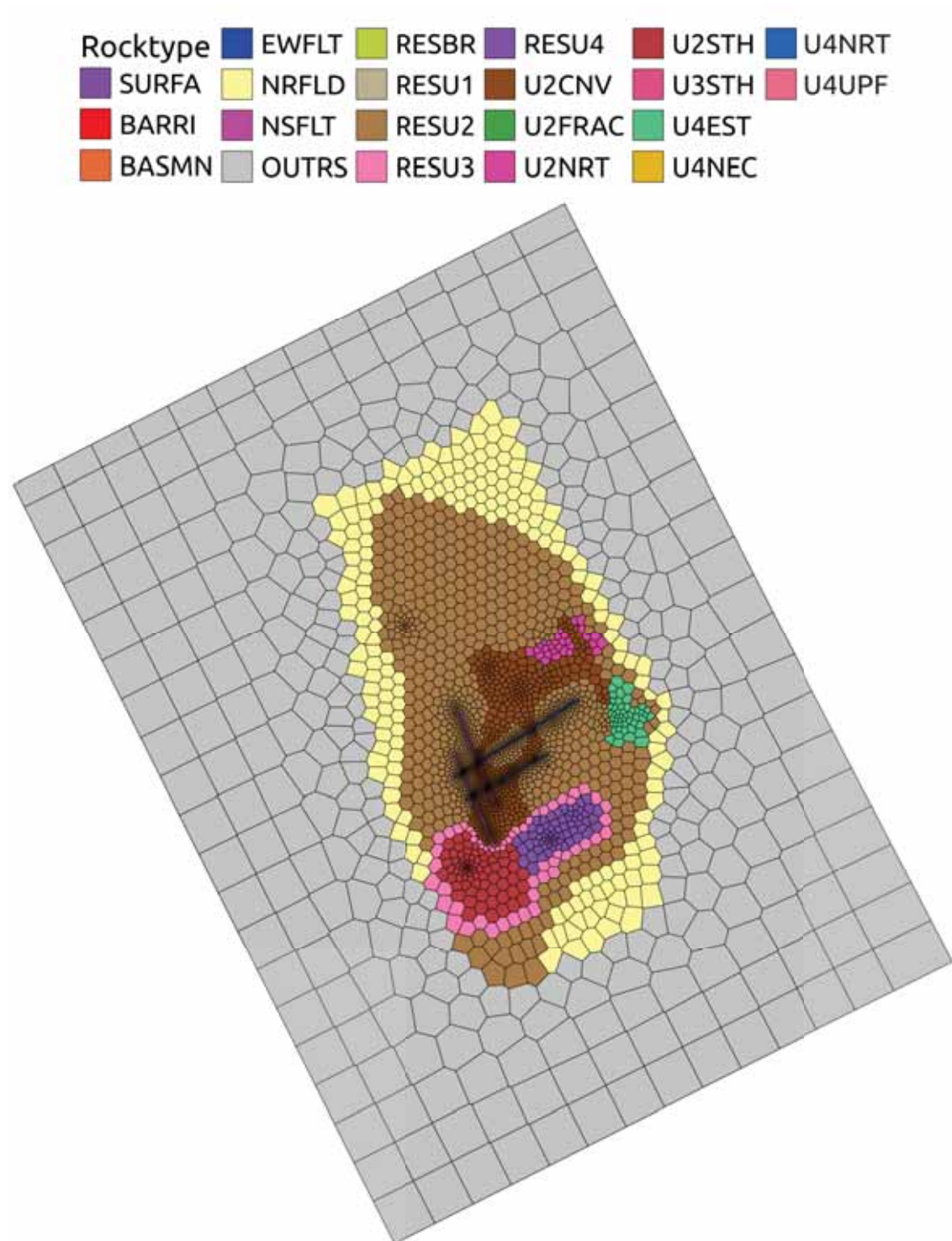
Figure A.6: Layer H.

Figure A.7: Layer Q.